



# Computational modeling of transitional flow over NACA-0018 airfoil at low Reynolds Number

Mohannad Y. Al Orabi

[orabimohannad@windowslive.com](mailto:orabimohannad@windowslive.com)

Ain Shams University, Cairo, Egypt

Nabil A. Mahmoud

[nabil\\_mahmoud@eng.asu.edu.eg](mailto:nabil_mahmoud@eng.asu.edu.eg)

Ain Shams University, Cairo, Egypt

Ahmed M. R. Elbaz

[ahmed.elbaz@bue.edu.eg](mailto:ahmed.elbaz@bue.edu.eg)

The British University Cairo, Egypt

Ashraf M. Hamed

[ashraf.mostafa@eng.asu.edu.eg](mailto:ashraf.mostafa@eng.asu.edu.eg)

Ain Shams University, Cairo, Egypt

## ABSTRACT

*The present study presents the computational modeling of transitional flow over NACA-0018 airfoil at low chord Reynolds number of  $10^5$  at various angles of attack ranging from  $0^\circ$  to  $15^\circ$  using two-dimensional Reynolds-averaged Navier-Stokes equations (RANS) combined with the Menter's ( $\gamma - \tilde{Re}_\theta$ ) transition model. Two different computational domain configurations were optimized in order to investigate the effect of the wind tunnel walls on the developed flow. The structured mesh technique was used for the both domains in order to generate high quality grids that obtain the turbulence model requirements. The numerically predicted results of the airfoil aerodynamic forces presented in terms of lift and drag coefficients as well as boundary layer predictions including surface pressure distribution, skin friction coefficient, mean velocity profiles, RMS velocity profiles and the boundary layer displacement thickness were compared to the experimental data. Very good agreement was attained prior the airfoil stall angle, whereas the agreement became poorer as the airfoil was completely stalled.*

**Keywords:** Aerodynamics, NACA-0018 airfoil, Transition modeling, Low Reynolds number airfoils, CFD.

## 1. INTRODUCTION

Recent technological progress in several fields including wind energy, aeronautics and astronautics applications represented in small-to-medium scale wind turbines, unmanned aerial vehicles and modern airships propulsion engines arise researchers special concern with the analysis of low Reynolds number airfoils which is generally used in such applications [1], [2]. Precise prediction of the airfoil aerodynamic characteristics represented mainly in the lift to drag ratio is considered the main key step for a successful design of various engineering devices that run under this condition.

Generally, experimental and computational procedures are commonly used for these studies. Each of these methods has its own features and drawbacks with different complexities and accuracy. Modern experimental techniques have the advantage of high accuracy in obtaining the realistic physical phenomenon. On the other hand, experimental testing represents a high cost burden of experimental setup and measuring equipment. Computational fluid dynamics (CFD) is considered one of the most extensively used techniques for designing and optimization of various aerodynamic devices, especially during the primary design phase. While CFD methods do not need any physical setup and can produce a lot of data by solving the governing flow equations, it also suffers the difficulty of modeling special flow phenomenon, such that, transition and turbulence. Further, performing high fidelity CFD simulations require very powerful computational resources.

At low Reynolds numbers, the flow over an airfoil slows down on the wall due to the viscous effects near the wall region producing a laminar boundary layer with relatively low kinetic energy. This boundary layer is exposed to additional pressure forces due to the presence of the airfoil surface curvature which in turn leads this layer to detach the surface [3]. This phenomenon is known as laminar separation [4]. At sufficiently low angles of attack and due to momentum exchange between the boundary

layer and the free-stream, this shear layer obtains higher kinetic energy and may reattach the airfoil surface as a turbulent boundary layer. A laminar separation bubble (LSB) forms between these two points of laminar separation and turbulent reattachment resulting in reversed rotational flow region and the flow is considered transitional. Although the turbulent boundary layer has fewer tendencies to separate than the laminar boundary layer because of its higher momentum, at higher angles of attack, the reattached turbulent boundary layer is subjected to turbulent separation near the airfoil trailing.

Experimental measurements of laminar to turbulent transition were reported for flow over airfoils by many authors. Timmer [5] studied the transitional flow over NACA-0018 airfoil. He reported lift coefficient measurements for angles of attack from  $0^\circ$  to  $30^\circ$  and Reynolds number ranging from  $1.5 \times 10^5$  to  $10^6$ . Nakano et al. [6] also reported measurements of a NACA-0018 airfoil at low Reynolds number. They reported surface pressure measurements and velocity measurements. Yarusevych et al. [7]–[9] have examined the boundary layer and turbulent wake development on a NACA-0025 airfoil at AOA =  $0^\circ$ ,  $5^\circ$ , and  $10^\circ$  for Reynolds numbers ranging from approximately  $50 \times 10^3$  to  $2 \times 10^5$ . Gerakopulos et al. [10] investigated flow characteristics for NACA-0018 for Reynolds numbers ranging from  $80 \times 10^3$  to  $200 \times 10^3$  and angles of attack from  $0^\circ$  to  $18^\circ$ . They recognized two distinct regions in the lift curves where in one region of rapid and linear growth of the lift coefficients existed at low angles of attack and in the second region more gradual and linear growth at higher pre-stall angles was observed. Furthermore, the slope of the lift curve in each region was found to be linked to the rates of change in separation, transition, and reattachment locations with the angle of attack. Boutilier and Yarusevych [11] reported experimental measurements of flow around NACA-0018 airfoil at low Reynolds numbers and investigated the effect of the experimental setup on the obtained results. They studied the effect of end plates and test-section blockage at Reynolds number of  $10^5$ . They confirmed the importance of using end plates to obtain uniformity of flow and minimize vortex-shedding. Blockage effects were studied by using an adaptive-wall test-section. They showed that high blockage ratios cause errors in lift as high as 9% of the maximum lift. The results of their investigations are used in the present work in order to examine the performance of transition turbulence model in predicting the airfoil aerodynamic characteristics at low Reynolds number.

In order to accurately predict the airfoil aerodynamic characteristics, it is recommended to use a turbulence model that is able to model the transition phenomena associated with the airfoil flow as the fully turbulent models computations will wrongly predict the aerodynamic performance [12], [13]. Menter et al. [12] introduced the so called  $(\gamma - \tilde{R}e_\theta)$  transition model that uses the local correlation approach for transition prediction which allows calibrated prediction of the transition onset and the transition extent for different transition mechanisms.

Various previous successive numerical studies also have been conducted for similar conditions including airfoil flow using the same model and proved the model ability to precisely predict the flow behavior around airfoils. Khayatzadeh and Nadarajah [14] employed the transition model to simulate the transitional flow around two different typical wind turbine profiles (S809 & NLF(1)-0416) for high Reynolds number conditions ( $Re > 2 \times 10^6$ ) at different angles of attack showing good agreement with experimental data for sectional lift, drag and moment coefficients. Fagbenro et al. [15] calibrated the default  $(\gamma - \tilde{R}e_\theta)$  transition model constants for a circular arc airfoil flow and compared the results with experimental data.

Haseeb et al. [16] used the  $(\gamma - \tilde{R}e_\theta)$  transition model for typical small wind turbines airfoil at low Reynolds number. Morgado et al. [17] showed that the  $(k-k_l-\omega)$  transition model provides more accurate results than the fully turbulent  $(k-\omega)$  SST model for high lift airfoils at low Reynolds number. Kapsalis et al. [18] compared three different transition models applied on NACA 0012 airfoil at high Reynolds numbers conditions and showed better agreement with experimental results than fully turbulent calculations without transition prediction.

The  $(\gamma - \tilde{R}e_\theta)$  transition model has been calibrated and validated against several transition flow conditions including zero pressure gradient and non-zero pressure gradient test cases which makes this model a good choice to use for the present study [19].

## **2. THE COMPUTATIONAL MODEL**

### **2.1 The Computational Domain**

Optimizing the computational domain is considered the first key element to simulate accurately the flow around the airfoil. Two different domains were in the current study to compare the results with the experimental work conducted in the University of Waterloo adaptive wall wind tunnel [11], [20]–[22]. A 2D rectangular straight wall bounded domain which have the same dimensions of the wind tunnel test section was used in the current study in order to simulate the realistic developed flow in the experimental setup considering the wind tunnel blockage ratio variations at different airfoil angles of attack as well as to include the effect of the tunnel walls on transition. Another domain was considered to simulate an open field domain as the upper and lower boundaries were located at a distance of  $15C$ , where  $C$  is the airfoil chord length, from the airfoil. In both cases, the inlet and outlet boundaries were located at a distance of  $10C$  and  $20C$ , respectively, from the airfoil. These distances are recommended in order to achieve the fully developed flow upwind and to be able to completely resolve the developed wake downwind. Figure 1 and figure 2 show the dimensions of wall bounded domain and the open field domain, respectively, as well as the adopted boundary conditions.

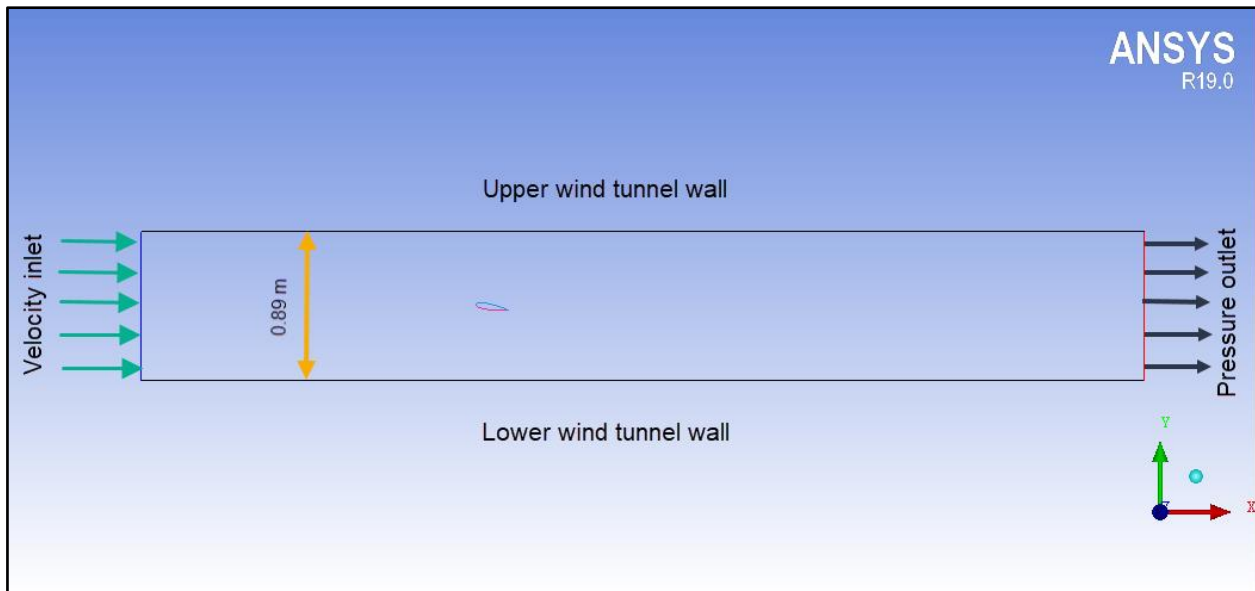


Figure 1: Wall bounded domain.

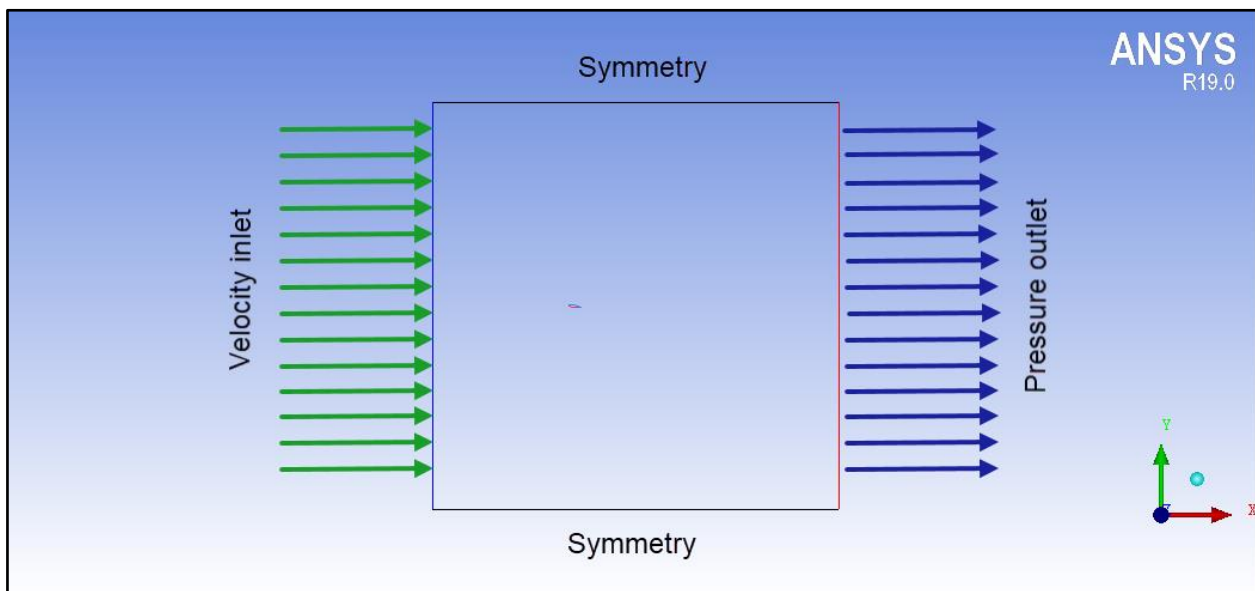


Figure 2: Open field domain.

## 2.2 Mesh Generation

Efficient spatial discretization of the optimized domain was generated as a result of various tests and trials. The meshing of the entire domain was divided into different sub domains using ANSYS ICEM grid generator. The strategy of multi block structured grids was applied in order to successively reach the optimum balance between fine grid density near the airfoil walls and the computational cost insuring smooth gradual growth of cell size between these sub domains to obtain better solution stability. High quality structured cells were obtained for all sub domains as the structured grid type has noticeable coding advantages over the unstructured grid type leading to better resolution and faster convergence. Figure 3 shows the generated mesh near the airfoil for different sub domains.

The grid independency study was carried out firstly on the open field domain at 10 degree angle of attack using three different levels of refinement and comparing the lift and drag coefficients results of each case until reaching the final grid independency solution as shown in table 1. Although different studies used less total number of cells in their studies accepting relatively minor errors [14], [16], the present study was performed using the fine mesh for all cases in order to exclude any errors that would result from the grid.

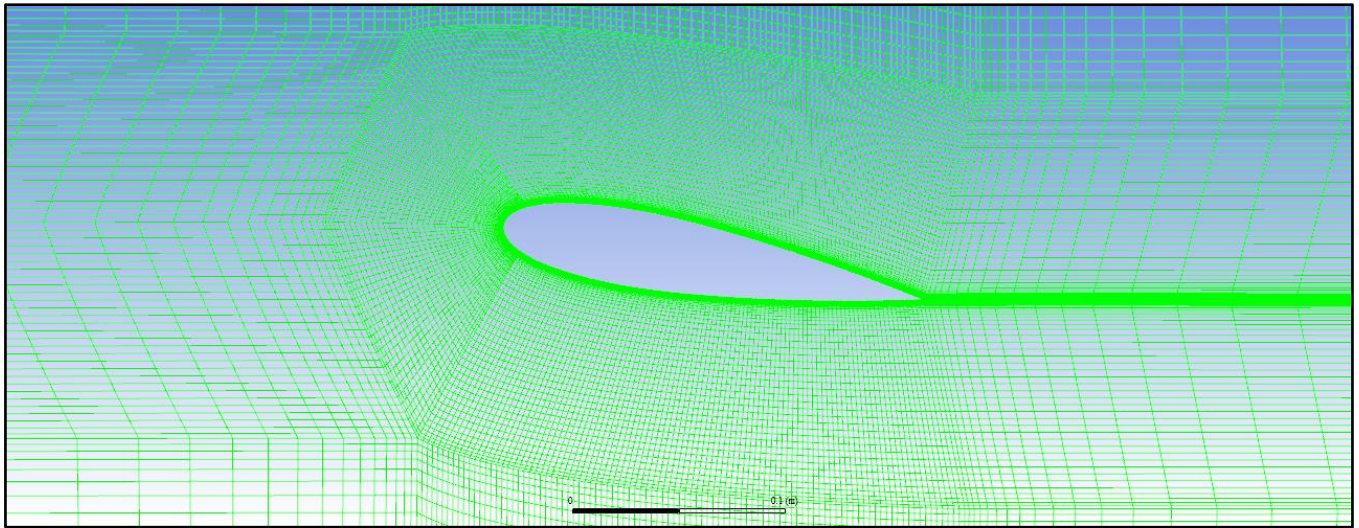


Figure 3: Close view to the airfoil grid topology at AOA=10°, the coarse mesh is presented.

Table 1: Grid independency test details.

| Mesh   | Boundary layer number of cells          |                                         |                 | Outer domain number of cells |        |            | Total number of cells | Results        |                |
|--------|-----------------------------------------|-----------------------------------------|-----------------|------------------------------|--------|------------|-----------------------|----------------|----------------|
|        | Number of cells along each airfoil side | Number of cells in transverse direction | Expansion ratio | inlet                        | outlet | Cross flow |                       | C <sub>L</sub> | C <sub>D</sub> |
| Coarse | 216                                     | 60                                      | 1.2             | 50                           | 100    | 50         | 325,314               | 0.7880         | 0.03625        |
| Medium | 575                                     | 100                                     | 1.1             | 100                          | 200    | 100        | 904,914               | 0.7854         | 0.03540        |
| Fine   | 1080                                    | 250                                     | 1.05            | 150                          | 300    | 150        | 1,193,814             | 0.7804         | 0.03635        |

For the wall bounded flow, the fine mesh was applied using all same parameters except the grids between the airfoil and the tunnel walls which were refined one more time using 250 grids for each side of the outer domain zone only. This extra refinement step was needed to insure that the previous optimized cell size was able to simulate correctly the flow interaction between the airfoil and tunnel walls without affecting the accuracy of the solution. The results were almost identical with an error of less than 0.2% in the lift and drag coefficients, so the previously optimized fine mesh was generated for all wall bounded cases also for its lower computational cost.

As an important recommendation of the transition turbulence model and best practices is to set the first cell height near the wall to obtain a the non-dimensional distance of the first cell near the wall ( $y^+$ ) value of less than unity [23], [24]. This approach is required to be able to fully resolve the viscous sub layer involved with low Reynolds number airfoil flow, where  $y^+$  is defined:

$$y^+ = \frac{y u_\tau}{\nu} \tag{1}$$

The  $u_\tau$  is the so called friction velocity,  $y$  is the first grid distance from the wall and  $\nu$  is the kinematic viscosity. This condition requires that  $y = 1 \times 10^{-5}$  m. for all simulated angles of attack according to the present Reynolds number.

### 2.3 Numerical Procedures

The inlet velocity used to reach the specified Reynolds number was set to 7.3 m/s. and its direction was maintained horizontally for all presented simulations, while the airfoil angle of attack was adjusted for each desired angle of attack by the same way as the experimental test procedures by rotating the airfoil around an origin point that is located at (0.3 C). The turbulence parameters boundary conditions at the inlet were optimized in order to match the experimental measured turbulent intensity at the airfoil leading edge were ( $Tu = 0.3\%$ ,  $\frac{\mu}{\mu_\tau} = 10$  ).

The steady-state pressure based solver of ANSYS FLUENT 19.0 was used for all computations. The pressure / velocity coupling was achieved using the SIMPLE algorithm produced by Patankar and Spalding [25]. The second order upwind scheme was used to approximate the face values of the transport equations convection terms for all variables [26] . Using this technique besides avoiding orthogonality between streamlines and mesh sides are recommended to minimize numerical diffusion [27]. For each computation, all results were obtained after reaching the quasi-state solution and the solution is considered to be converged as the residuals for all flow and turbulence parameters are below  $10^{-6}$  , this can be actually achieved for the fine mesh after 20,000 and 30,000 iterations, depending on the angle of attack.

**2.4 Turbulence Model**

The  $(\gamma - \tilde{R}e_{\theta})$  transition model introduced by Menter et al. [12] was chosen in the present study. The model formulation uses the  $(K - \omega)$  SST turbulence model [28] combined with two transport equations for transition prediction: one for the intermittency  $(\gamma)$  to predict transition locally and one for the local transition onset momentum thickness Reynolds number  $(\tilde{R}e_{\theta})$  which is used to account for the nonlocal turbulence intensity effects.

**3. Results and Discussion**

The transition model was applied to predict the flow behavior around the NACA-0018 airfoil at Reynolds number of  $10^5$  at various angles of attack of 0, 5, 8, 10 and 15 degrees. The results including airfoil aerodynamic forces represented by the lift and drag coefficients, surface pressure distribution, skin friction coefficient, mean velocity profiles, RMS velocity profiles and the boundary layer displacement thickness are compared with the experimental measurements.

Figure 4 and figure 5 show the predicted variation of lift and drag coefficients respectively for both the open field domain and the wall bounded domain, compared with experimental results. As can be seen, we can find that the predicted lift coefficients of the wall bounded domain have higher values over these predicted using the open field domain. Both values are showing good agreement with the measured experimental results [11]. Otherwise, the drag coefficients for both tested domains seem to be almost identical before the airfoil experimentally observed stall condition ( $AOA \leq 11^\circ$ ). After stall, for  $AOA=15^\circ$  there is a noticeable difference between both predicted values. Comparing the predicted drag coefficient values to the measured experimental data [29] we can notice that for  $AOA = 0^\circ$  and  $5^\circ$  the predicted values are showing good agreement with the experimental results, but for higher angles of attack the present model underestimates the drag coefficient by a remarkable value that increases with increasing the angle of attack.

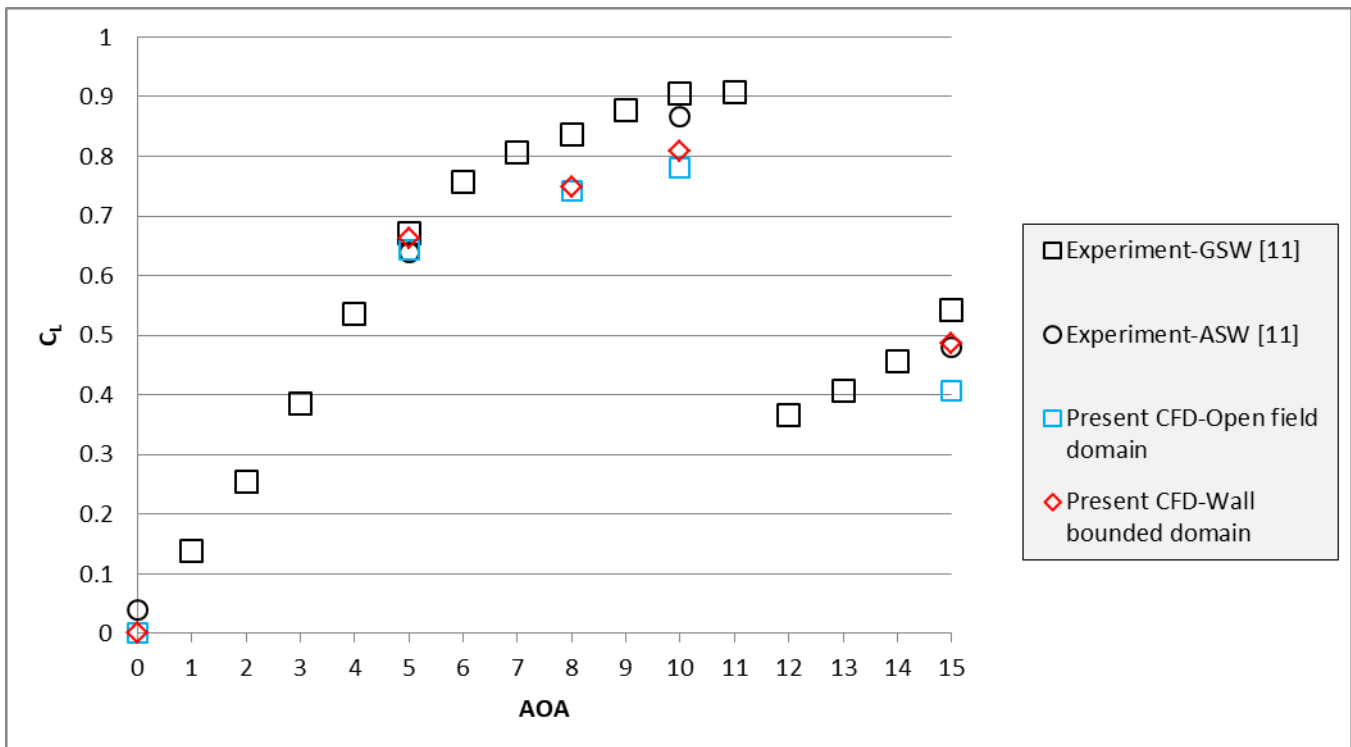


**Figure 4:** Comparison between experimental and numerical results of the lift coefficients for both domain configurations.

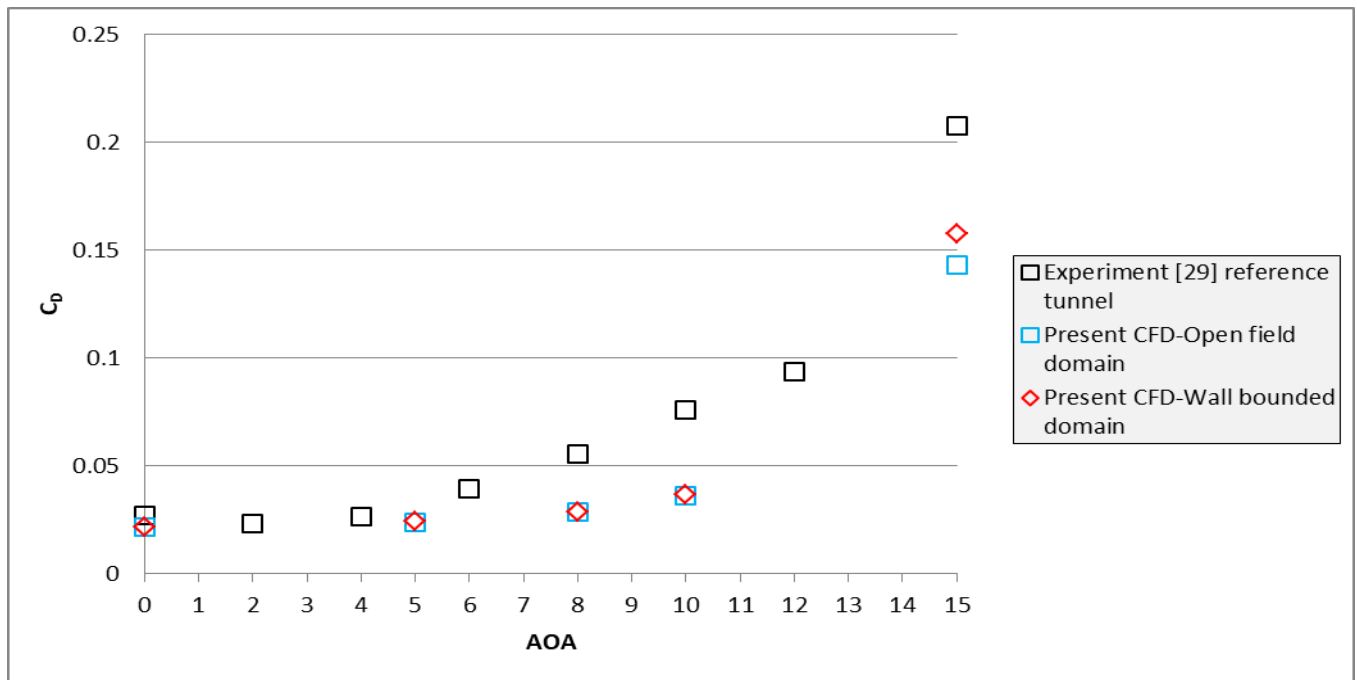


Figure 5: Comparison between experimental and numerical results of the drag coefficients for both domain configurations.

Table 2 shows quantitative comparison between the predicted lift and drag coefficients for both domains. Comparing these values together, we can notice that, for small angles of attack ( $AOA \leq 10^\circ$ ) the difference between both lift and drag coefficients can vary only by almost relatively small values that correspond to a minor deviation of (2-3.5) % only, but for higher angles of attack ( $AOA = 15^\circ$ ) the deviation is dramatically large which represent a large deviation between lift coefficients of 16% and between drag coefficients of more than 10%. This is expected due to the increase of the blockage ratio for higher angles of attack.

Table 2: Airfoil predicted aerodynamic coefficients values for both domains.

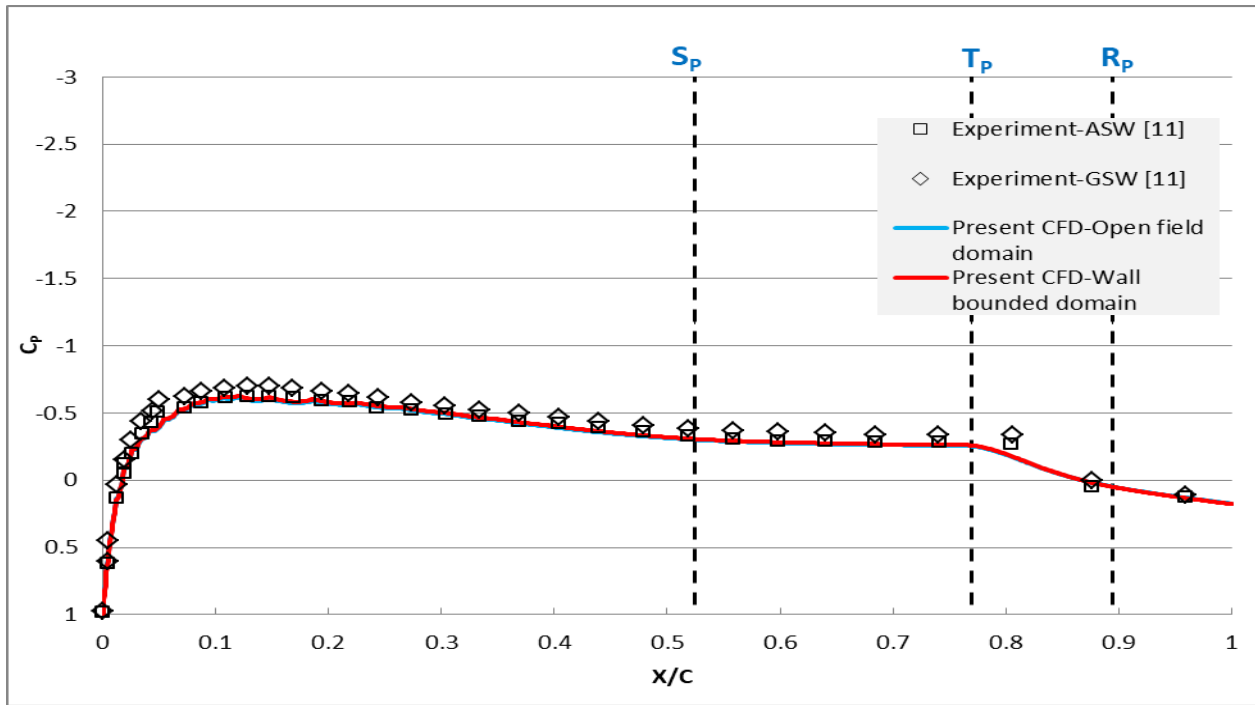
| AOA | Open Field Domain |          | Wall Bounded Domain |         | Variation in predicted Lift (%) | Variation in predicted Drag (%) |
|-----|-------------------|----------|---------------------|---------|---------------------------------|---------------------------------|
|     | $C_L$             | $C_D$    | $C_L$               | $C_D$   |                                 |                                 |
| 0   | 0.00086           | 0.0215   | 0.0008              | 0.022   | 7.5                             | 2.3                             |
| 5   | 0.643             | 0.024    | 0.66357             | 0.0246  | 3.2                             | 2.5                             |
| 8   | 0.7429            | 0.02898  | 0.7492              | 0.0294  | 0.85                            | 1.45                            |
| 10  | 0.78037           | 0.036345 | 0.809               | 0.037   | 3.67                            | 1.8                             |
| 15  | 0.407             | 0.143    | 0.486               | 0.15759 | 19.4                            | 10.2                            |

Before the stall angle for an airfoil that is generally operating at low Reynolds numbers the aerodynamic flow characteristics over the airfoil suction side can demonstrate the trend of the pressure distribution. As the free stream flow reaches the airfoil leading edge, the surface curvature causes the flow to accelerate resulting in a peak suction pressure then the laminar sub-layer beyond the airfoil surface slows down due to the presence of wall shear stress which results the peak suction pressure to be partially recovered reaching nearly constant pressure zone that indicates the formation of laminar separation bubble towards the transition point. Just after the transition point, a strong pressure recovery takes place until the reattachment point where the flow returns turbulent. According to such criteria, the whole pressure plateau can be used to identify separation ( $Sp$ ), transition ( $Tp$ ) and reattachment ( $Rp$ ) points. This technique has been previously used for airfoil flow [30]. The separation point is characterized by a constant pressure zone whereas the transition point is characterized by the start of sharp pressure drop. Subsequently downstream, the reattachment point is characterized by linear pressure drop behavior over the airfoil. On the other side, after the stall angle, the airfoil is considered completely stalled and the trend of the pressure distribution becomes dramatically different.

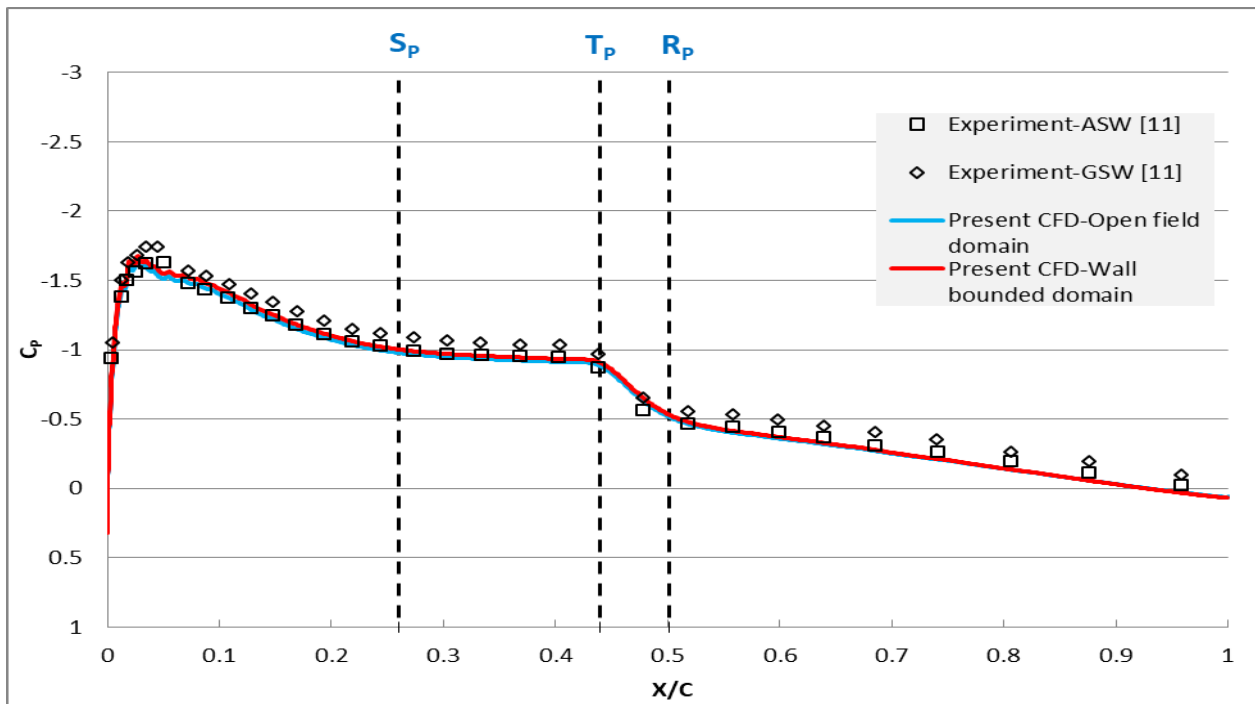
The predicted surface pressure distributions over the airfoil suction side for angles of attack from 0 to 15 degrees were obtained for both different domain configurations and compared with the measured experimental results, figure 6. Using the above definitions and the plotted pressure plateau over the airfoil suction side, we can identify the expected separation, transition and reattachment locations  $Sp$ ,  $Tp$  and  $Rp$ , respectively, for each angle of attack. These locations are listed accurately and compared with the measured experimental findings in table 3. From the experimental measurements for both GSW and ASW configurations we can observe that the existence of the wind tunnel upper wall causes relatively more suction pressure on the airfoil suction side by noticeable difference that increases slightly by increasing the angle of attack. This behavior is expected as a result of the

relatively small distance between the tunnel wall and the airfoil (2.225 C) which may lead to larger velocities. On the other side, the different experimental tunnel wall configurations do not affect any of the separation, transition and reattachment locations. Comparing the predicted surface pressure coefficients with the experimental data, before airfoil stall for  $AOA \leq 10^\circ$  the transition turbulence model produces the same trend for the surface pressure distribution over the airfoil as well as it can accurately predict the separation, transition and reattachment locations. On the other hand, after the stall angle,  $AOA=15^\circ$ , the transition model results are showing small deviation from the experimental results.

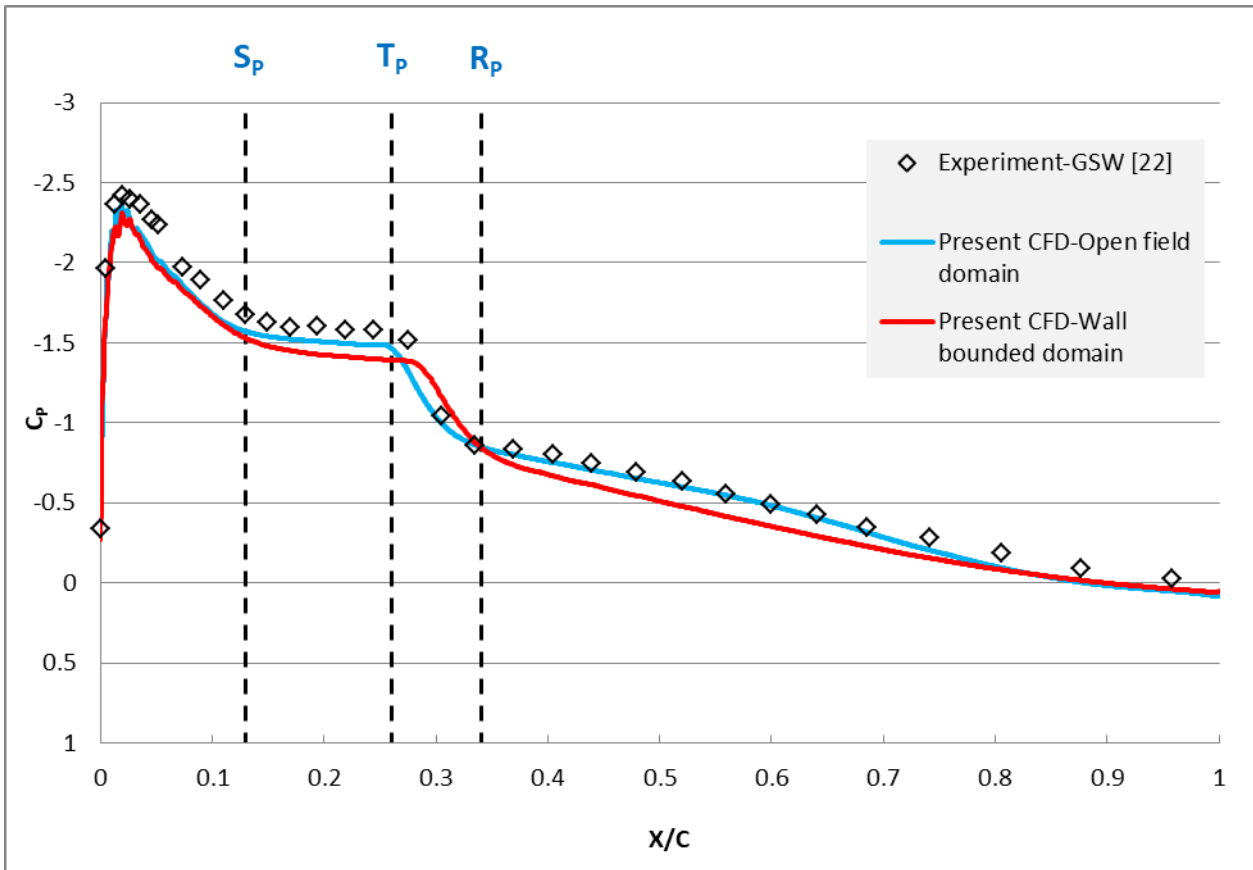
The obtained numerical model results for both tested domains are also presented showing that the model can predict minor variation in the surface pressure coefficient values due to the wall configuration. This variation can be obviously noticeable for high angles of attack due to the presence of higher blockage ratios while for small angles of attack ( $AOA=0^\circ$  and  $5^\circ$ ) this difference is too small. Nevertheless, the predicted separation, transition and reattachment locations using the two different domains are identical, so the simulated wall doesn't affect any of these predicted points and any variations of the predicted lift and drag coefficients are only due to the predicted variations in the surface pressure coefficient values due to the wall configuration.



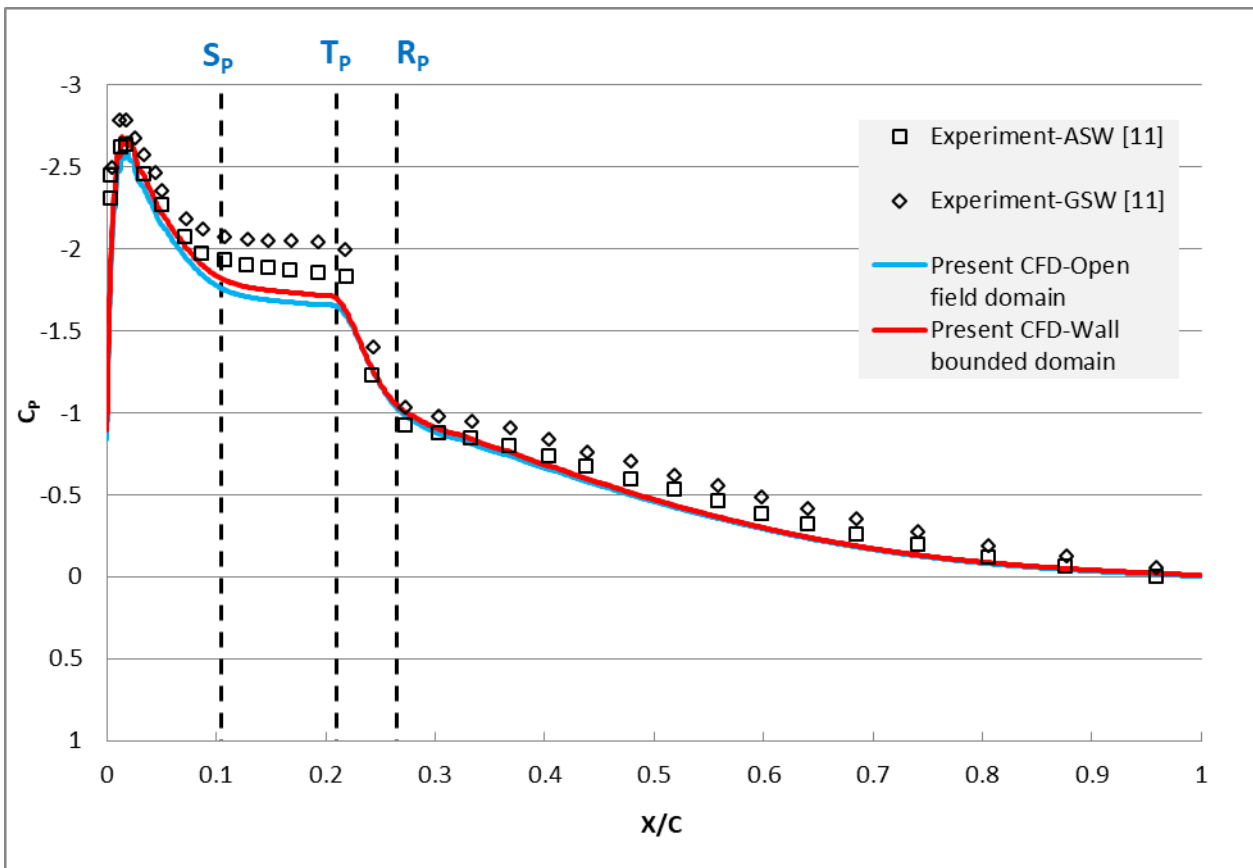
a.  $AOA=0^\circ$ .



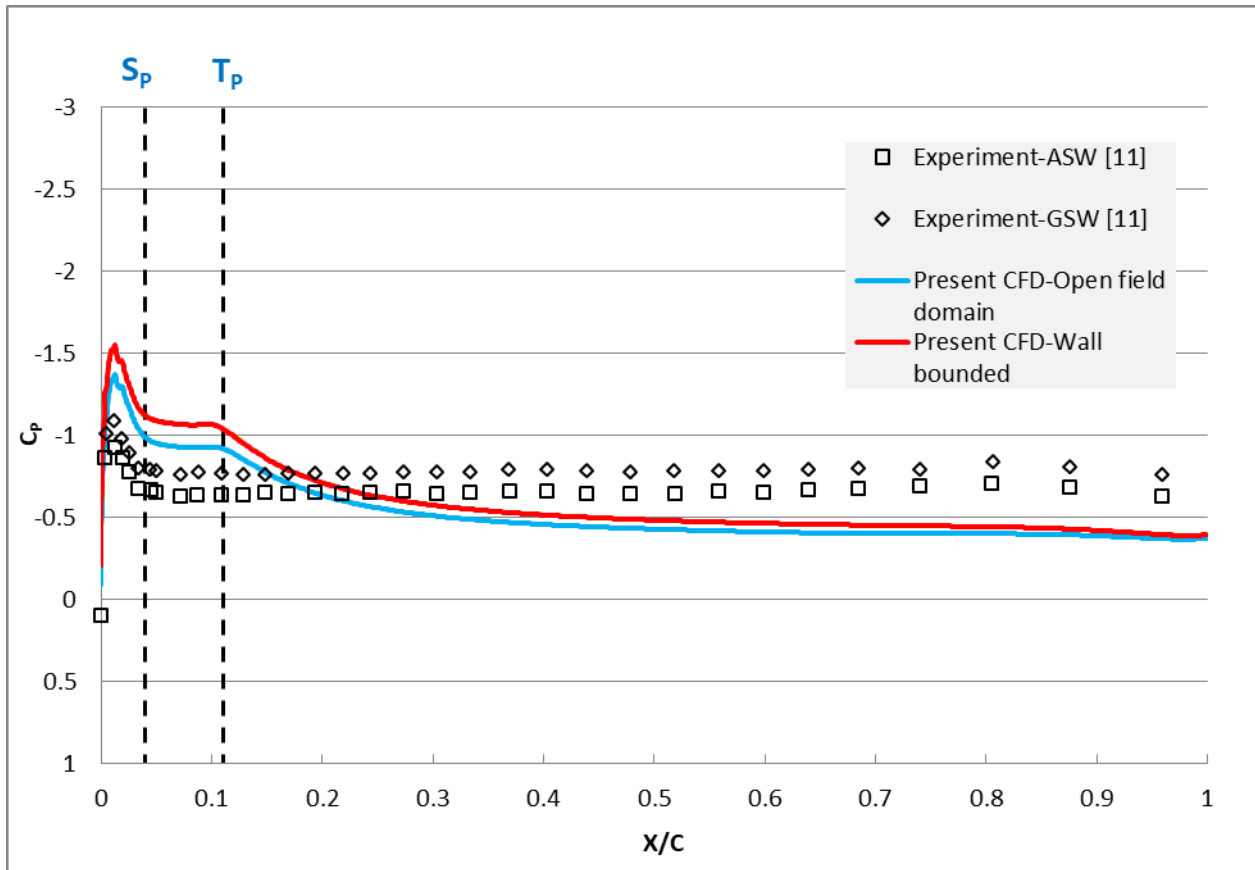
b.  $AOA=5^\circ$ .



c. AOA= $8^\circ$ .



d. AOA= $10^\circ$ .



e. AOA=15°.

**Figure 6:** Surface pressure coefficient distribution along airfoil suction side for different angles of attack.

**Table 3:** Mean separation, transition and reattachment estimated locations from surface pressure distribution and compared with experimental data [20], [22].

| AOA | X <sub>s</sub> /c |             | X <sub>T</sub> /c |             | X <sub>R</sub> /c |             |
|-----|-------------------|-------------|-------------------|-------------|-------------------|-------------|
|     | EXP.              | CFD-present | EXP.              | CFD-present | EXP.              | CFD-present |
| 0   | 0.52±0.02         | 0.525       | 0.8±0.035         | 0.77        | 0.88±0.04         | 0.894       |
| 5   | 0.24±0.015        | 0.26        | 0.44±0.02         | 0.44        | 0.52±0.02         | 0.501       |
| 8   | 0.13±0.01         | 0.13        | 0.27±0.015        | 0.26        | 0.33±0.018        | 0.34        |
| 10  | 0.09±0.01         | 0.105       | 0.22±0.013        | 0.21        | 0.27±0.015        | 0.265       |
| 15  | 0.038             | 0.04        | 0.194             | 0.11        | -                 | -           |

Comprehensively comparing all pressure distributions for all angles of attack together, we can notice that, as the airfoil AOA increases to the airfoil stall angle, the maximum suction pressure increases, whereas after stall, the trend of the pressure distribution on the airfoil suction side is somewhat different due to separation bubble burst and there is no reattachment occurs. That explains the significantly lower maximum suction pressure for AOA=15° than for AOA=10°.

In the presence of separation bubble formation, increasing the angle of attack actually causes the separation point to move towards the airfoil leading edge as well as the separation bubble extent is decreased. These observations are common for general airfoils which are operating at such low Reynolds numbers [30], [31].

After focusing on the pressure distribution analysis along the airfoil suction side as it considered the dominant parameter that is supposed to separation, the predicted numerical values of the surface pressure coefficients on the airfoil pressure side for both domains are also presented in figure 7 which have almost identical values for both open field and wall bounded domains. This observation is also recognized from the experimental data [11], so only the obtained open field domain results are compared with the ASW experimental data which show a very good agreement. We can summarize that the tunnel walls effect on the airfoil pressure side can be neglected experimentally and numerically.

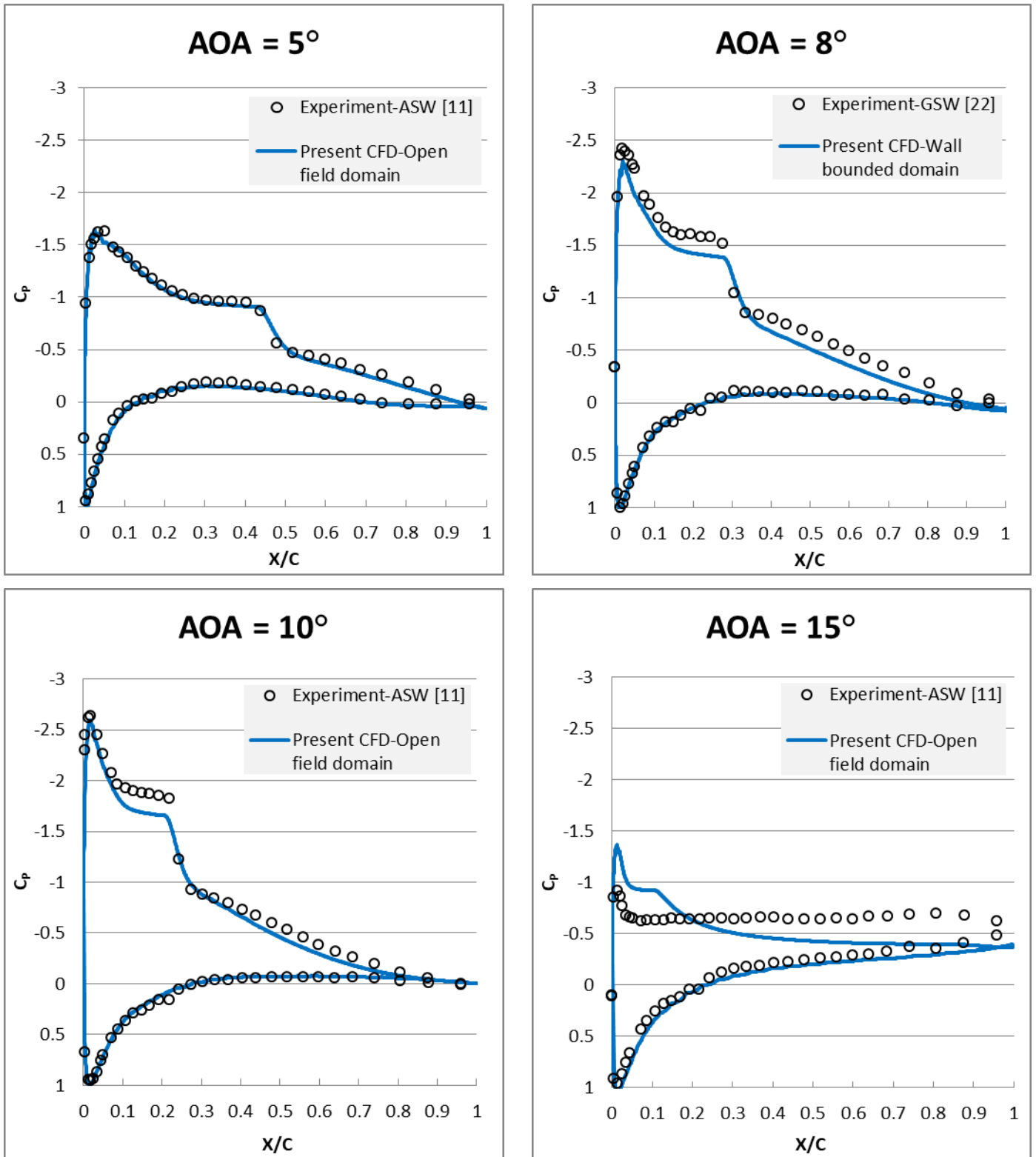


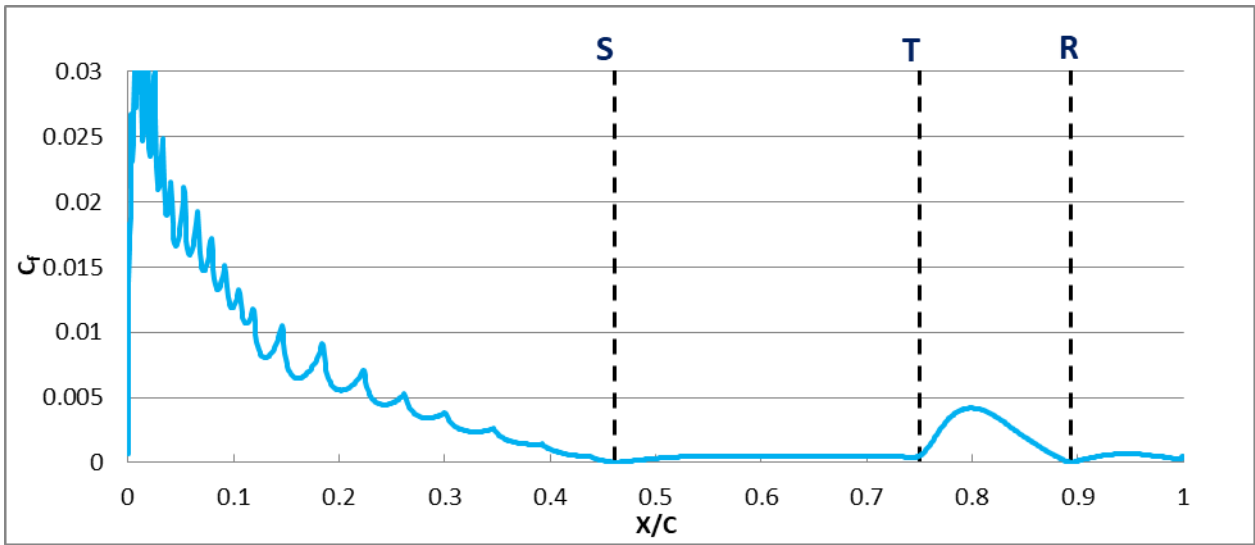
Figure 7: Surface pressure distribution for both airfoil sides. For similarity, AOA=0° is not presented.

The skin friction coefficient is defined as the ratio between the wall shear stress and the local dynamic pressure that can be expressed as follow:

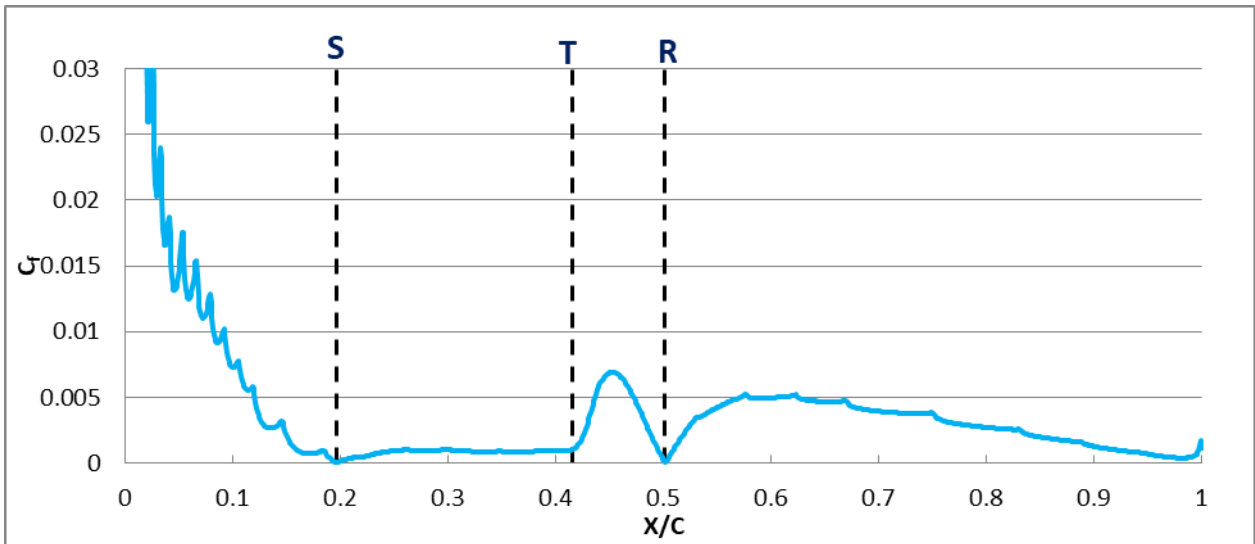
$$C_f = \frac{\tau_w}{\frac{1}{2}\rho U^2} \quad (2)$$

Practically, the wall shear stress developed by the boundary layer dies out across any inflecting point in the boundary layer where the shear stress changes sign because of the change in flow direction [32]. While at the transition onset location the skin friction coefficient begins to grow rapidly. Applying such technique to the plotted skin friction coefficient along the airfoil suction side we can determine precisely the separation, transition and reattachment locations. Since the numerical simulations of both open field and wall bounded domains are predicting typically identical values of the skin friction coefficient along the airfoil suction side for

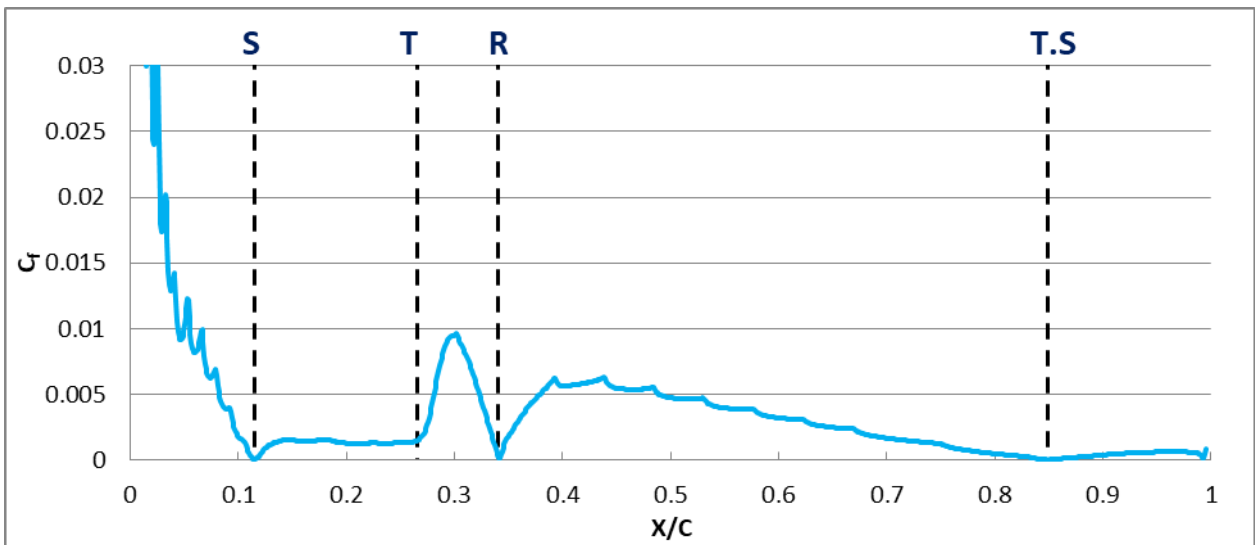
all simulated angles of attack. The predicted skin friction coefficients for all simulated angles of attack obtained from the open field domain are presented in figure 8.



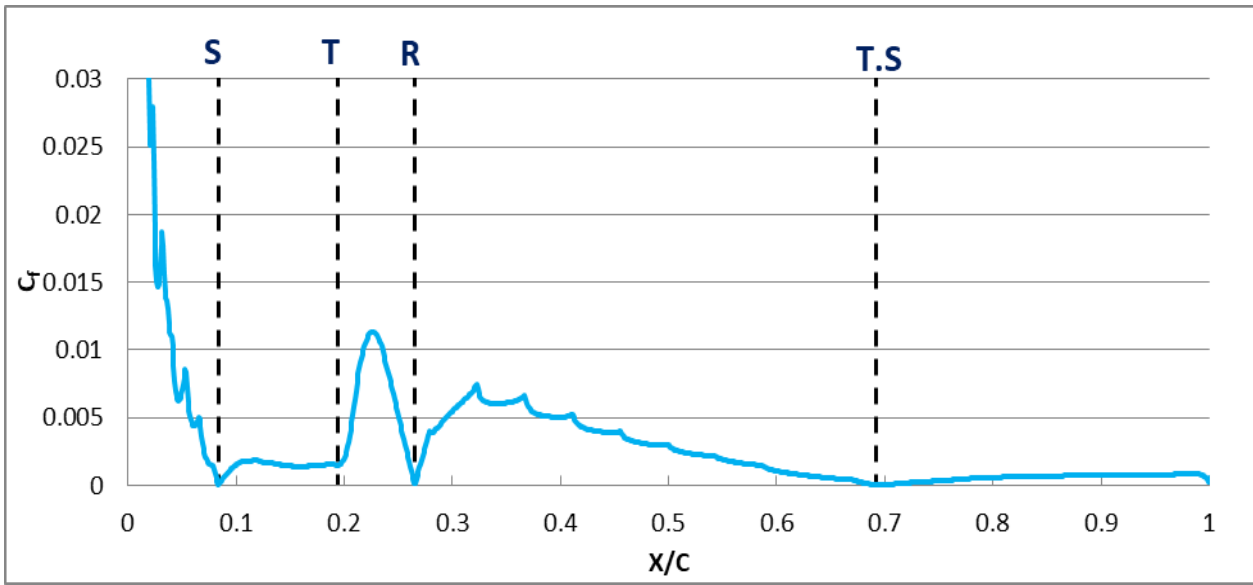
a. AOA= $0^\circ$ .



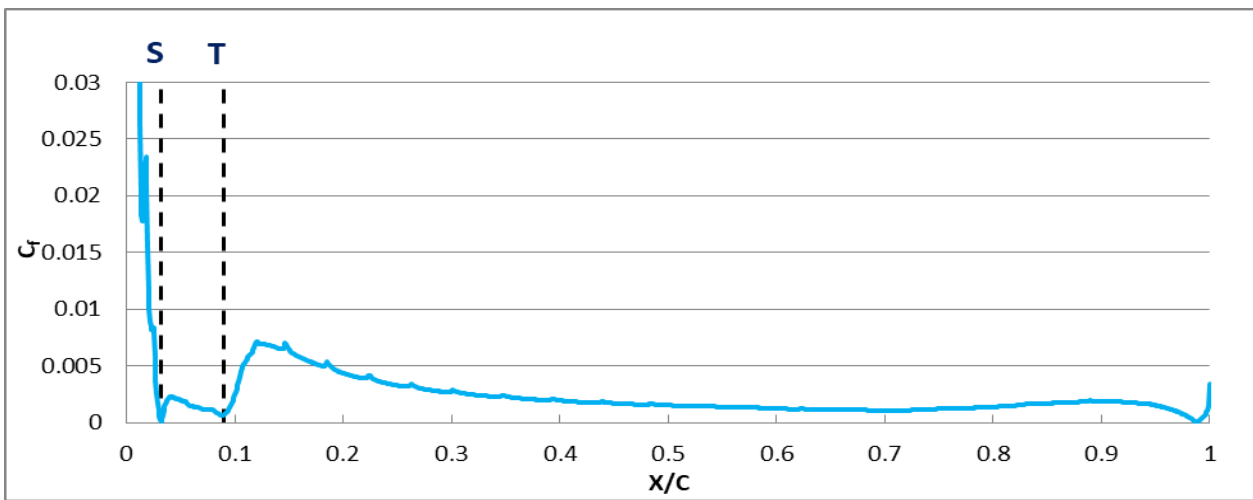
b. AOA= $5^\circ$ .



c. AOA= $8^\circ$ .



d. AOA=10°.



e. AOA=15°.

**Figure 8:** Predicted skin friction coefficient along airfoil suction side for different AOAs. Dash lines represent separation (S), transition (T), reattachment (R) and turbulent separation (T.S) points.

From a general overview of the flow characteristics over an airfoil surface, as the free stream reaches the airfoil leading edge the skin friction goes to its maximum value and then decreases to its first minimum value at the separation point (S) where the wall shear stress vanishes and then grows to almost a constant value along the separation bubble. The point where the skin friction coefficient begins to increase rapidly indicates the transition onset location (T) and then it goes again to its second minimum value that indicates the turbulent reattachment location (R) where the reverse flow vanishes [32]. If the skin friction coefficient reaches a third minimum point again, this inflection point presents the trailing edge turbulent separation location (T.S).

Comparing the actual separation, transition and reattachment locations which are obtained from the skin friction coefficient with these that have been estimated previously from the pressure plateau for all angles of attack, the actual separation and transition locations predicted from the skin friction coefficient occur more early than the estimated locations according to the pressure plateau concept, while the reattachment locations are the same. A more benefit of the skin friction coefficient plot that it can clearly predict the trailing edge turbulent separation point as for AOA=8° and 10° which is not noticeable from the pressure plots. A typical values comparison is presented in Table 4.

**Table 4:** Difference between separation and transition locations identified from Skin friction coefficient and pressure coefficient distributions.

| AOA | Skin Friction Coefficient |                   | Pressure Coefficient |                   | Deviation in separation prediction (%) | Deviation in transition prediction (%) |
|-----|---------------------------|-------------------|----------------------|-------------------|----------------------------------------|----------------------------------------|
|     | X <sub>S</sub> /c         | X <sub>T</sub> /c | X <sub>S</sub> /c    | X <sub>T</sub> /c |                                        |                                        |
| 0   | 0.4615                    | 0.75              | 0.525                | 0.77              | 12.095                                 | 2.597                                  |

|    |        |        |       |       |        |       |
|----|--------|--------|-------|-------|--------|-------|
| 5  | 0.1965 | 0.415  | 0.26  | 0.44  | 24.423 | 5.682 |
| 8  | 0.1145 | 0.265  | 0.13  | 0.266 | 11.923 | 0.376 |
| 10 | 0.0836 | 0.1937 | 0.105 | 0.21  | 20.381 | 7.762 |
| 15 | 0.0319 | 0.09   | 0.04  | 0.11  | 20.25  | 18.18 |

Mean velocity profiles are also plotted for each case at different streamwise locations in order to delve deeper in the velocity vectors inside the boundary layer verifying the associated reversed flow behavior inside the separation bubble. Figures 9-13 show the velocity profiles at different streamwise locations over the airfoil surface for all simulated angles of attack. For each angle of attack, the presented profiles demonstrate the typical manner of the flow over low Reynolds number airfoils. Precedes the point of separation, the developed attached laminar boundary layer is observed. Once the separation arises, the separated shear layer with reverse flow can be recognized near the wall. Downstream the reattachment point, the profile exhibits as attached turbulent boundary layer. Comparing the predicted model results with the measured experimental data, the used model is showing good agreement with the experimental data inside the attached laminar and turbulent boundary layers. For the reversed flow region inside the separation bubble there are some deviations between the numerical and experimental results, which can be explained due to the fact that the experimentally used normal hot wires cannot expose the direction of the flow [21], [33].

For AOA=0°, the velocity profile at X/C=0.28 indicates the laminar boundary layer developed due to the free stream flow facing the airfoil wall at the leading edge. Furthermore, the separation occurs downstream at X<sub>s</sub>/C=0.4615 as described before, so the reversed flow can be clearly observed for the profiles at X/C=0.6, X/C=0.8 and downstream the flow is recovered and reattached at X<sub>R</sub>/c=0.89, then the boundary layer becomes turbulent as for X/C=0.94. Similar behavior is found for all presented angles of attack with the difference of separation, transition and reattachment locations except for the AOA=15°, where there is no reattachment occurs and the flow exhibits reversed along the entire suction side after the separation point. Furthermore, for AOA = 10° additional flow behavior can be observed at X/C=0.87 where a small thin layer exhibits reversed flow after the reattachment point that verifies the previously observed turbulent separation near the airfoil trailing edge.

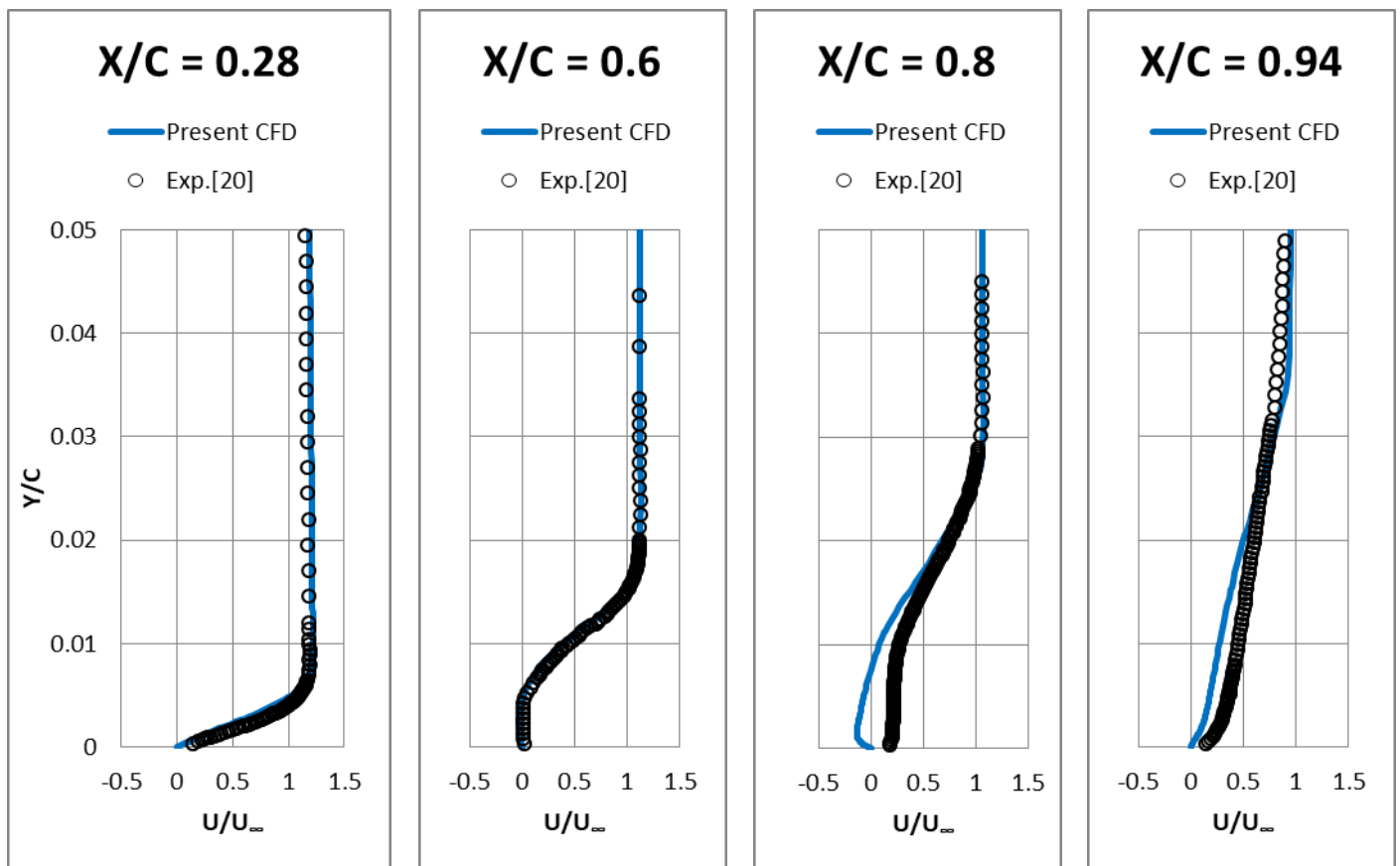


Figure 9: Mean velocity profiles at different streamwise locations AOA=0°.

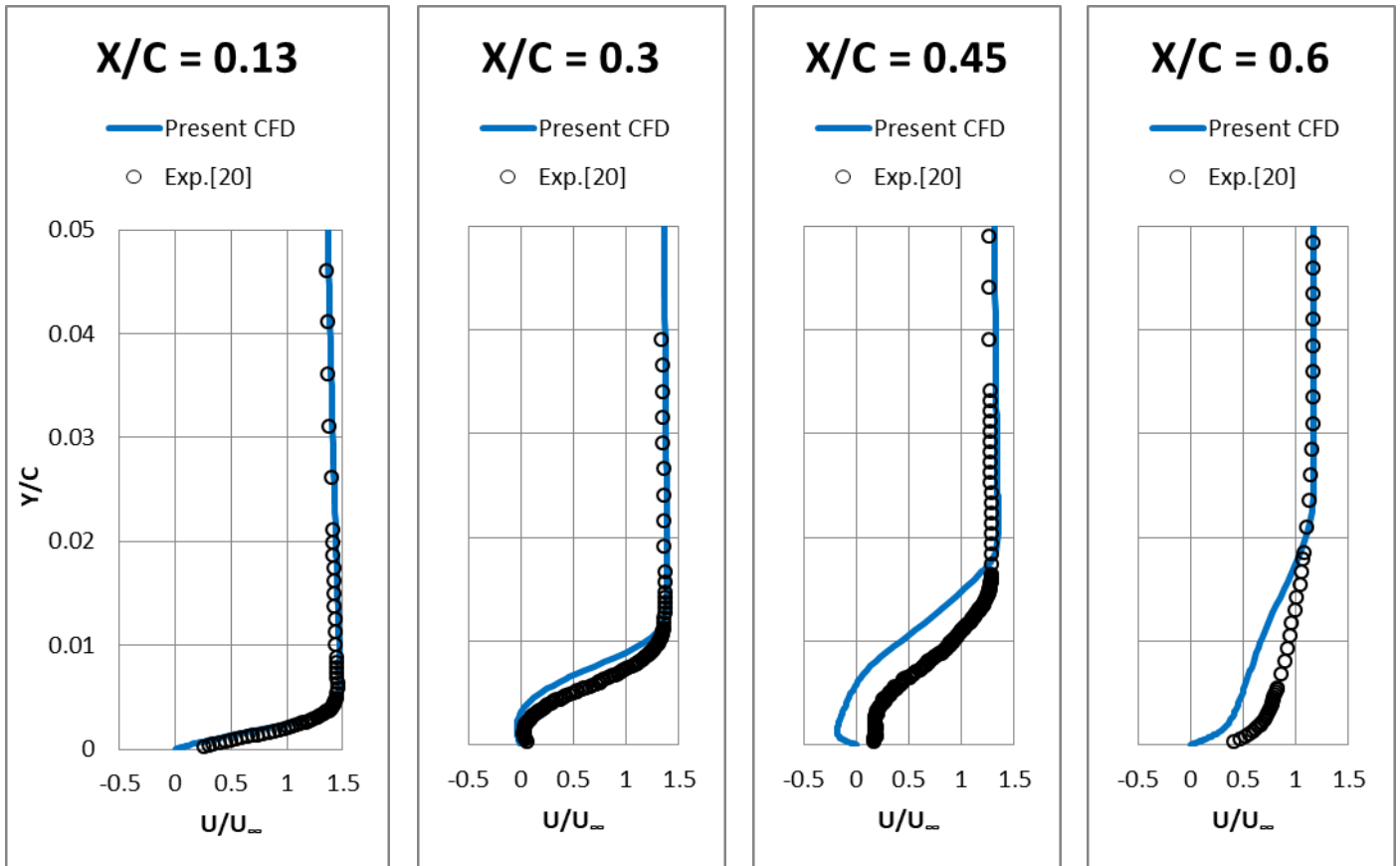
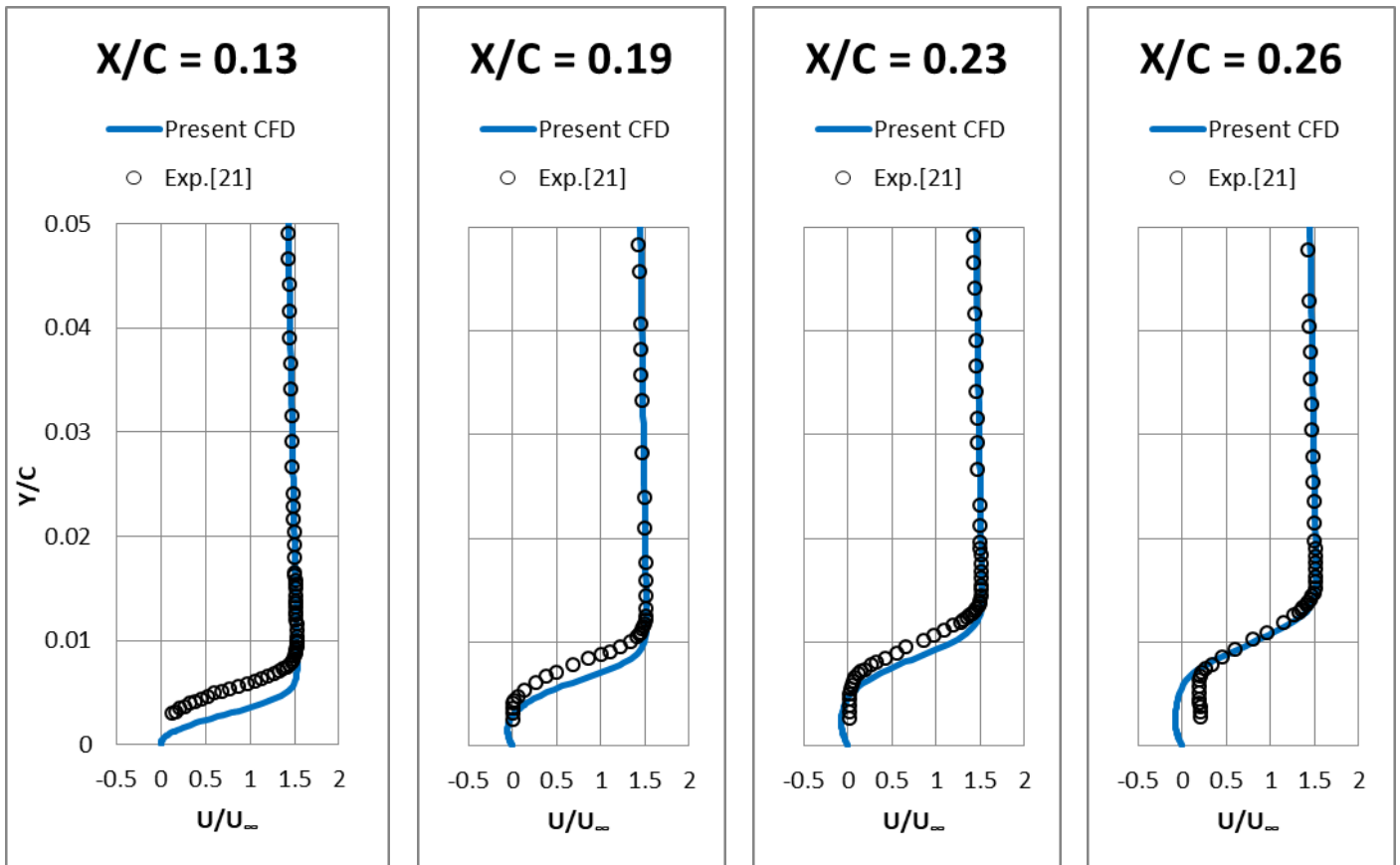


Figure 10: Mean velocity profiles at different streamwise locations  $AOA = 5^\circ$ .



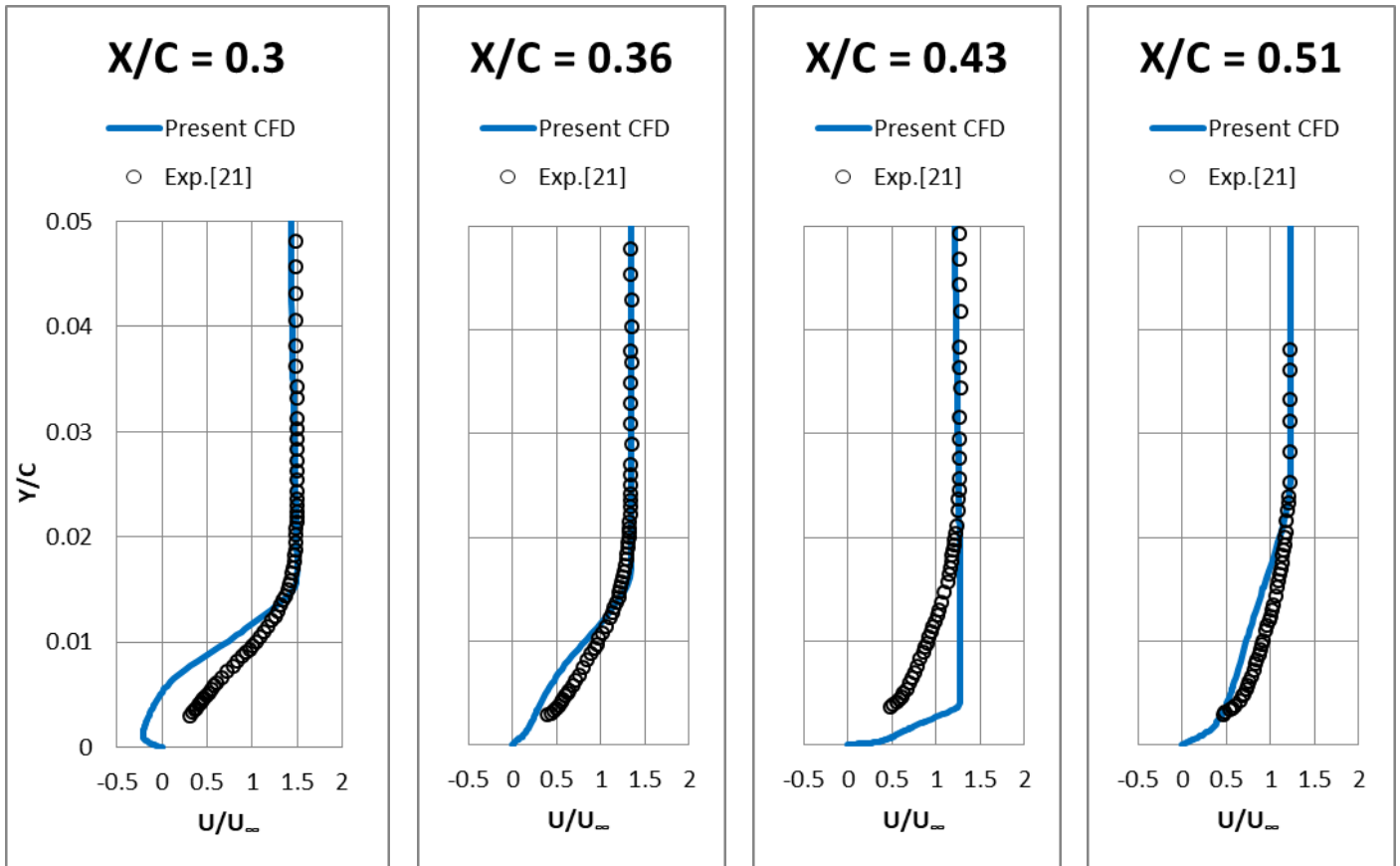


Figure 11: Mean velocity profiles at different streamwise locations AOA=8°.

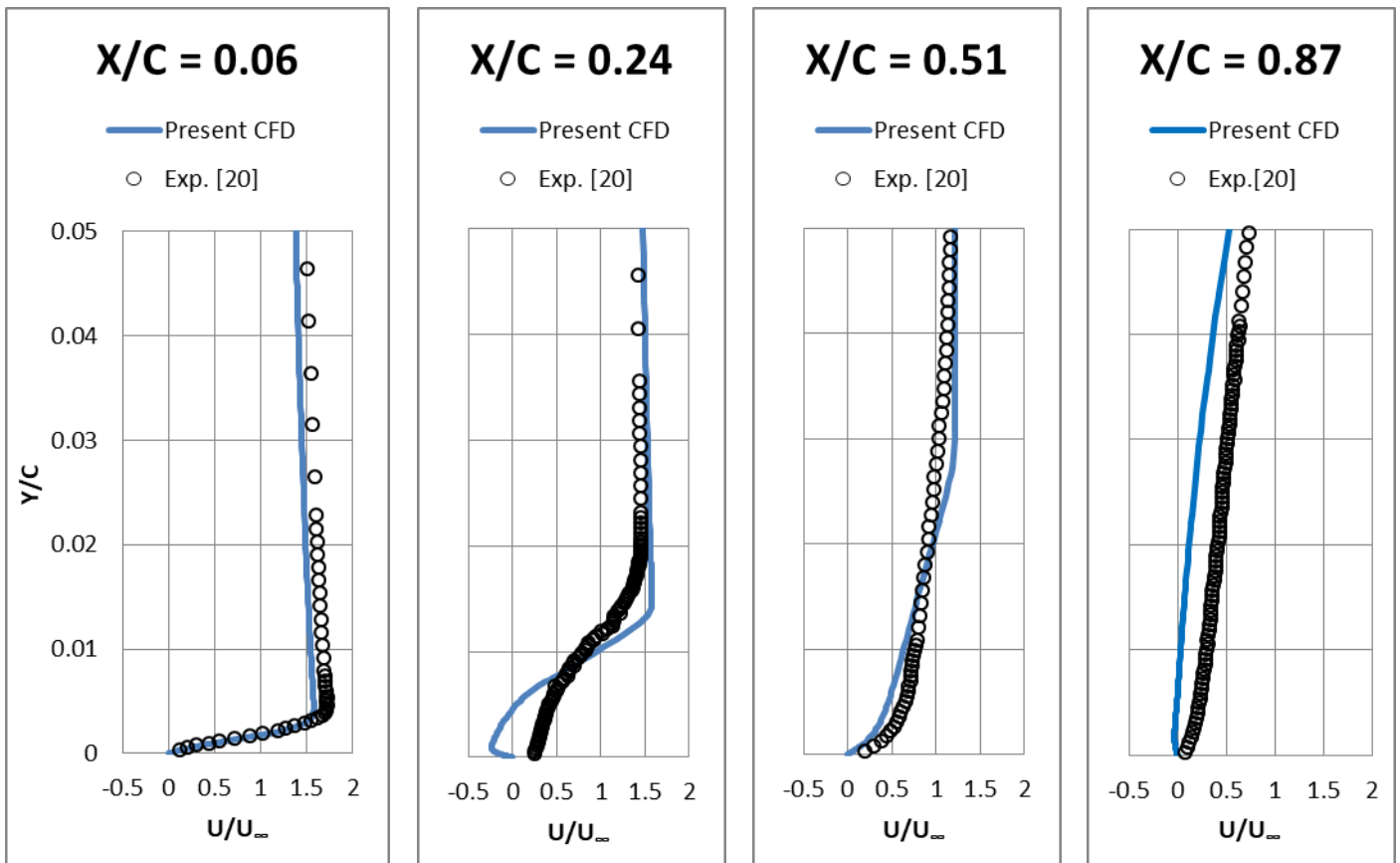


Figure 12: Mean velocity profiles at different streamwise locations AOA=10°.

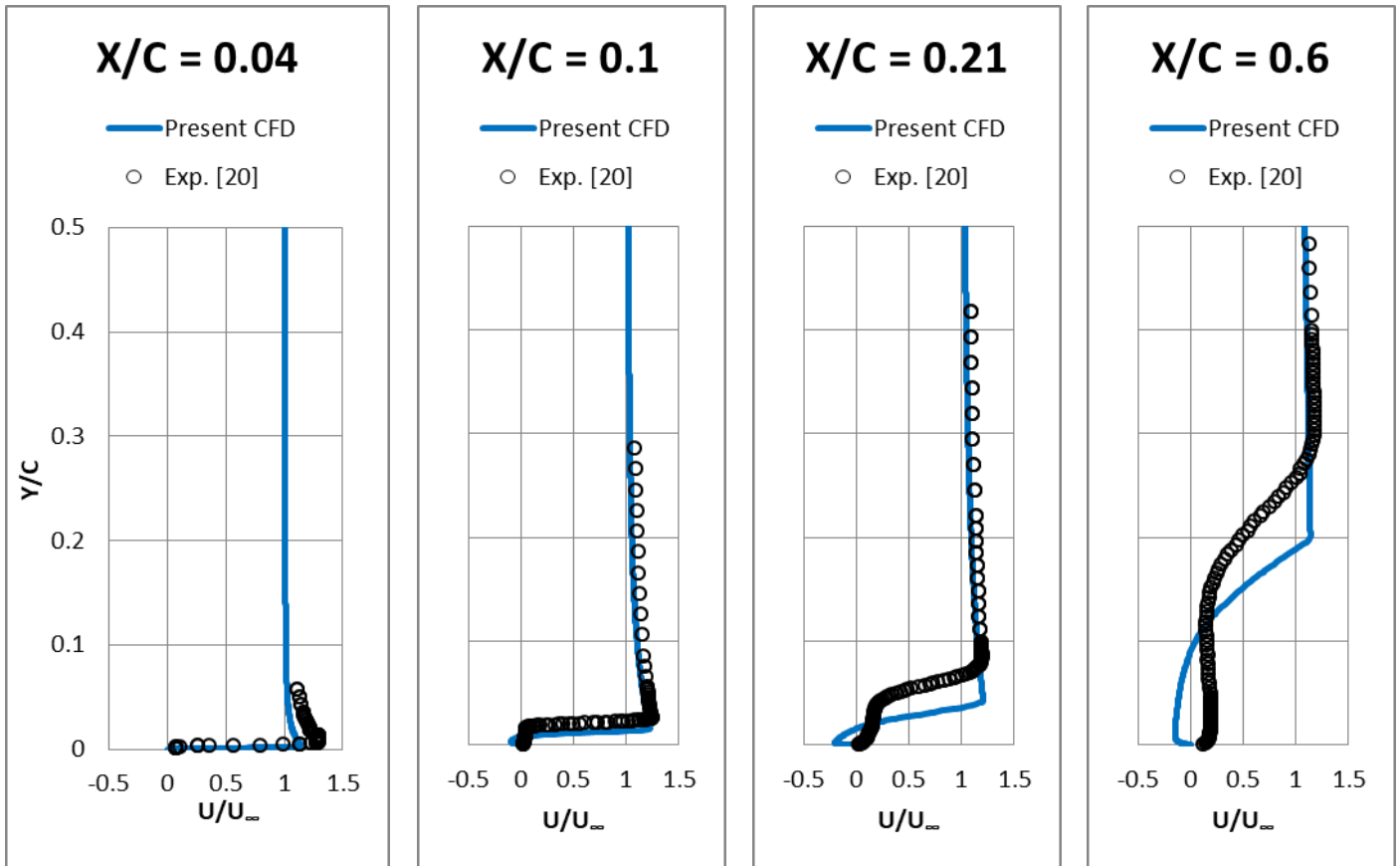


Figure 13: Mean velocity profiles at different streamwise locations AOA=15°.

The RMS velocity profiles have been calculated for each streamwise location from the obtained kinetic energy profiles as follow  $\tilde{u} = \left(\frac{2K}{3}\right)^{0.5}$  and the profiles are shown in figures 14-18 compared with experimental data. In the attached boundary layer the magnitude of the maximum obtained RMS velocity value in each profile is increased gradually. For the laminar separated flow region downstream the separation point, the RMS velocity profiles are presenting additional peaks as well as the amplitude of the fluctuations is showing rapid increase in the streamwise direction. However, in the reattached turbulent boundary layer the RMS velocity profiles have a single peak near the wall and decay more gradually into the free stream than in the laminar boundary layer upstream. Although the predicted profiles can recognize the same trend as the experimental profiles, the turbulence model is underestimating the values.

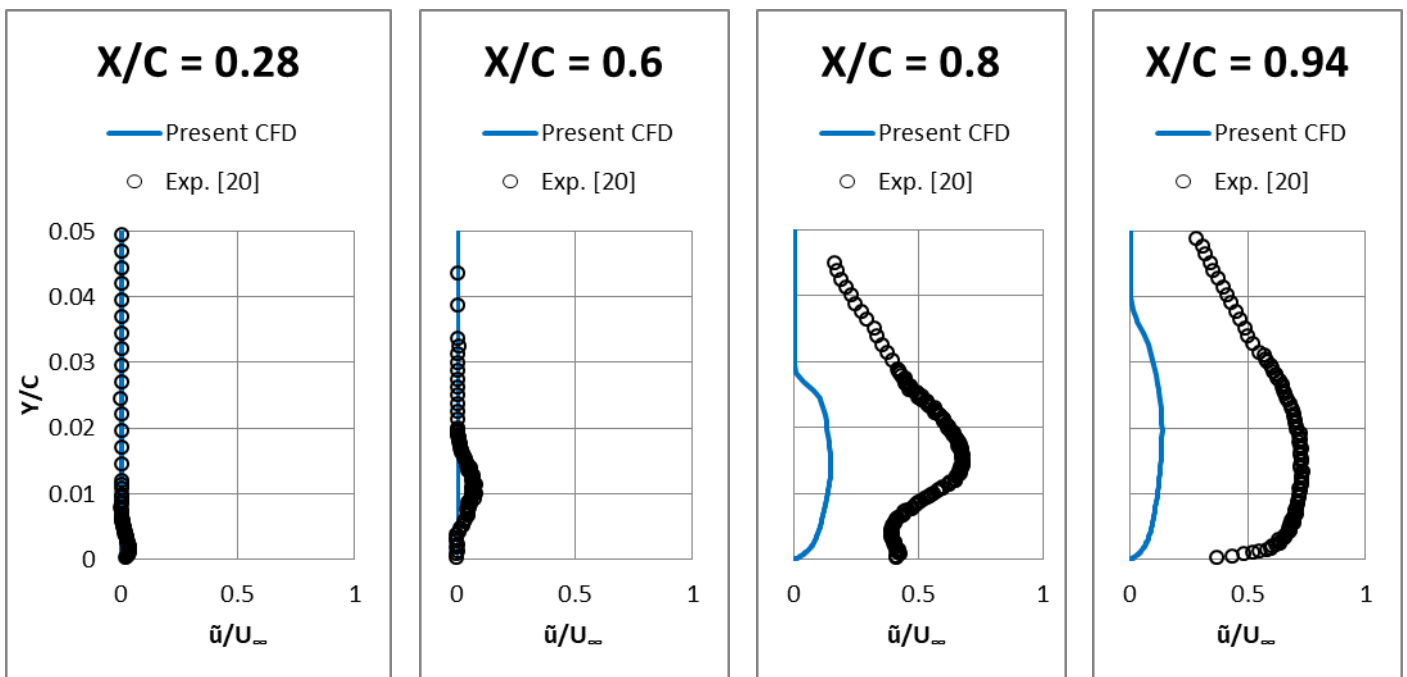


Figure 14: RMS velocity profiles at different streamwise locations AOA=0°.

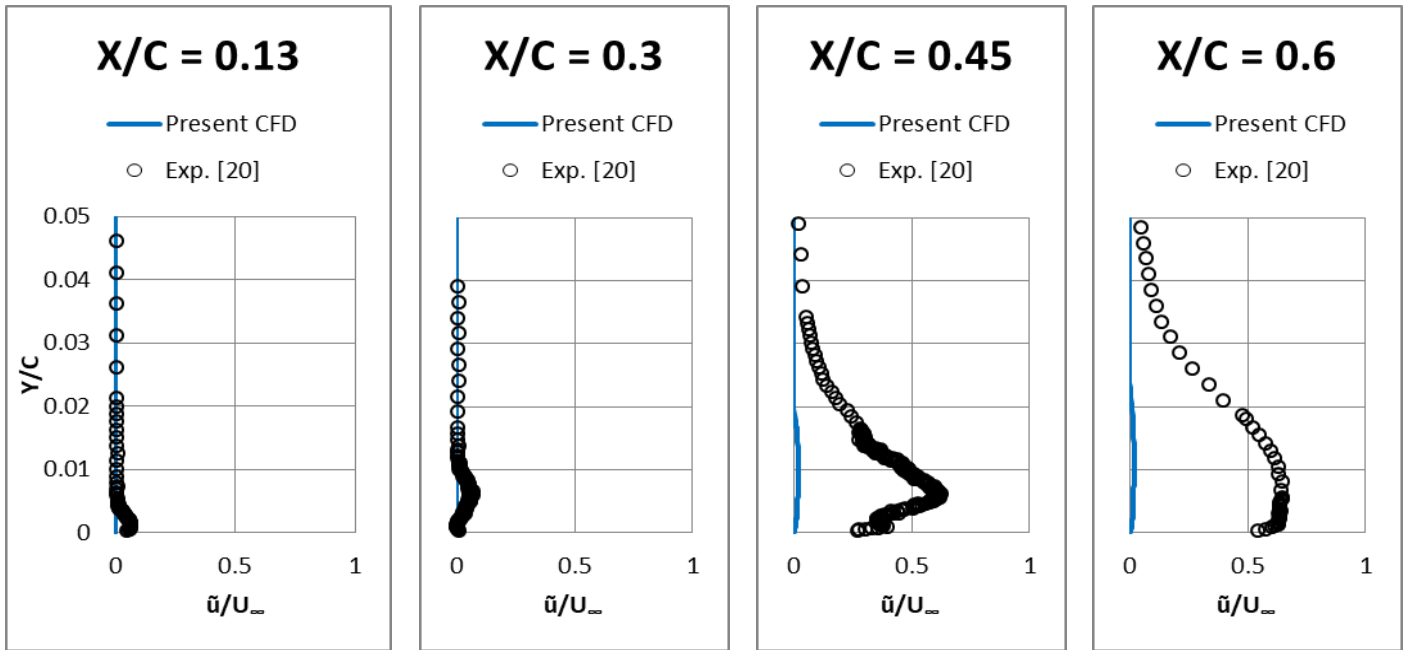


Figure 15: RMS velocity profiles at different streamwise locations AOA=5°.

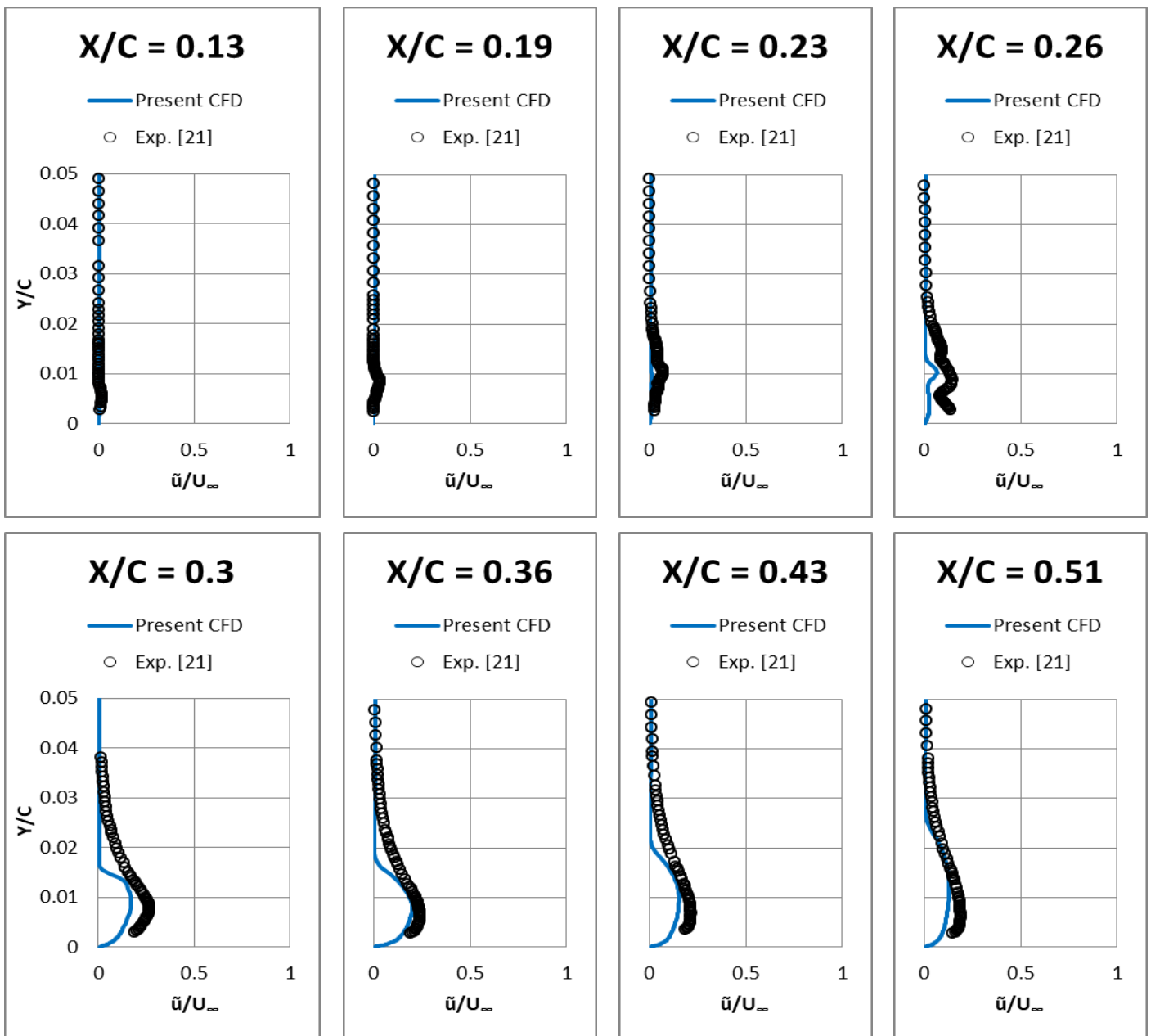


Figure 16: RMS velocity profiles at different streamwise locations AOA=8°.

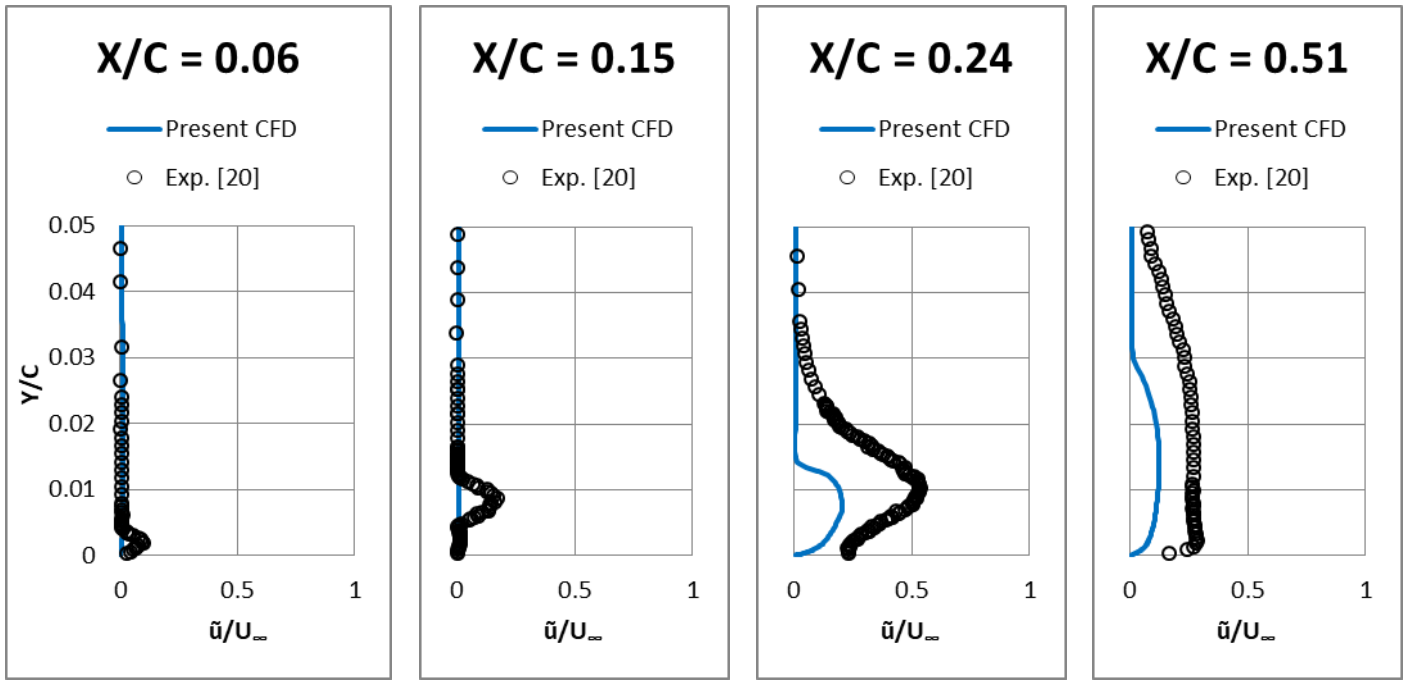


Figure 17: RMS velocity profiles at different streamwise locations AOA=10°.

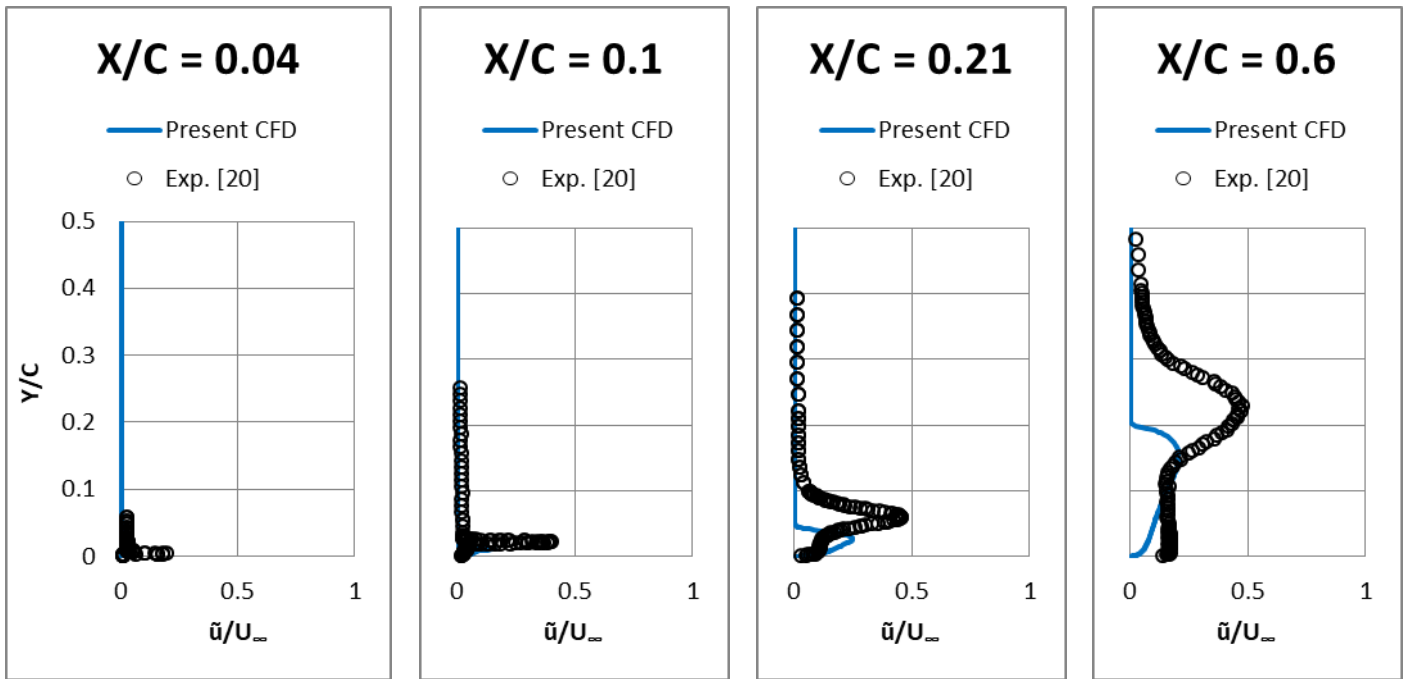
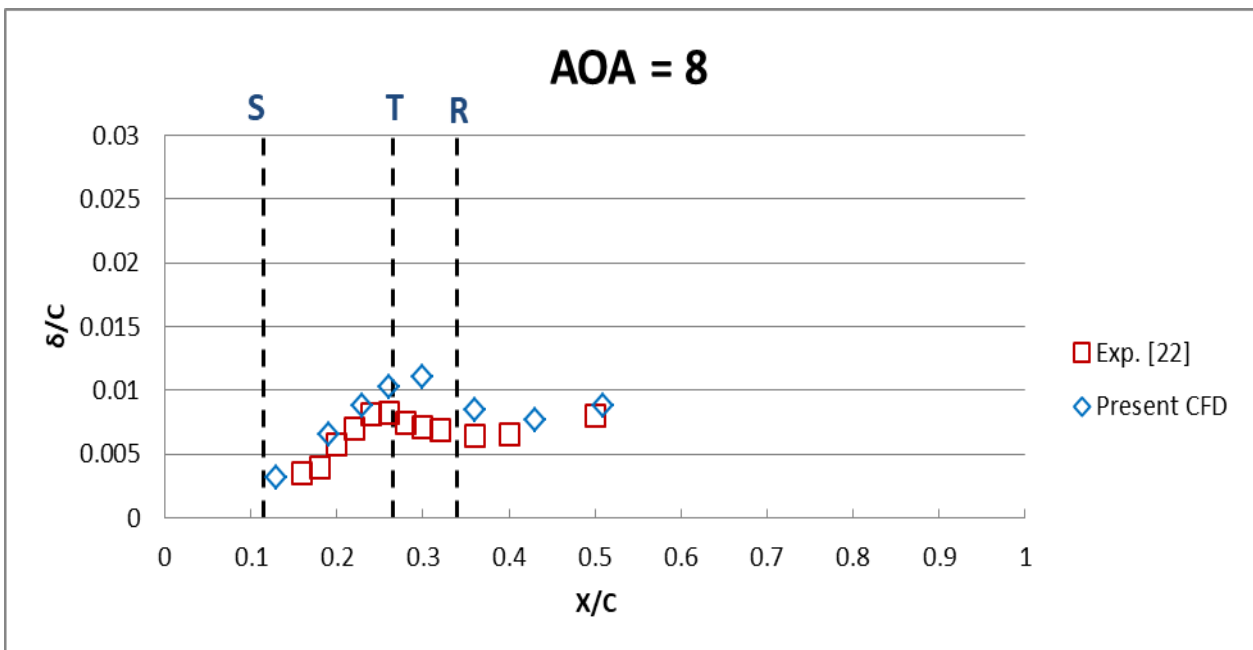
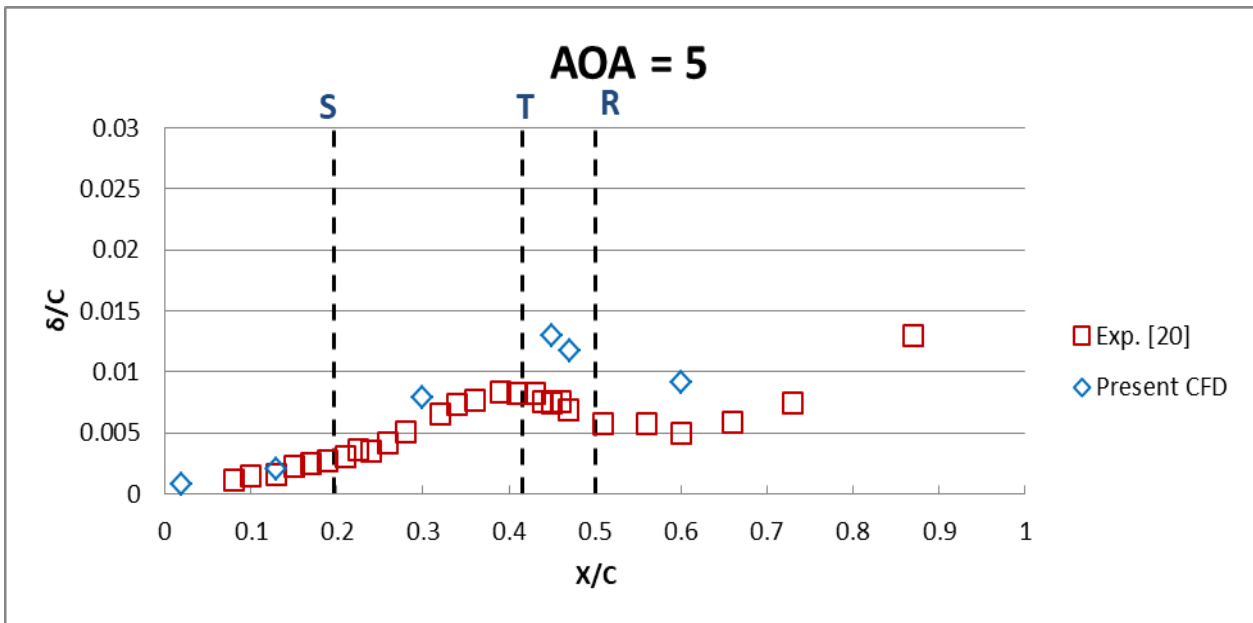
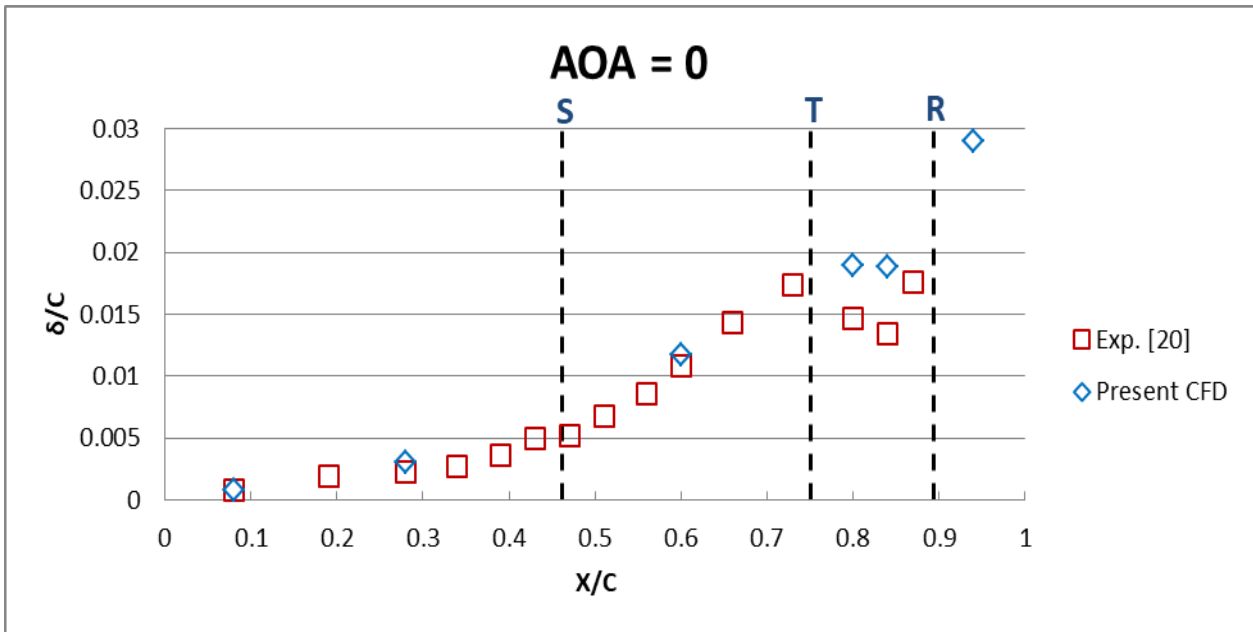


Figure 18: RMS velocity profiles at different streamwise locations AOA=15°.

The displacement thickness is defined as the distance by which the external potential flow is displaced outwards due to the reduction in velocity inside the boundary layer. It can be actually computed by integrating each velocity profile from the wall to the location of the edge velocity  $\int_0^{\delta_e} (1 - U/U_e) dy$ , where  $U_e$  is the edge velocity and was identified as the maximum velocity for each velocity profile. Figures 19 present the computed displacement thickness with the comparison to experimental data. From a comprehensive analysis for the plotted displacement thickness for all angles of attack before stall, displacement thickness increases slowly for the attached laminar boundary layer and is considered almost linear. The slope of the linear increase actually increases as the angle of attack is increased. Downward the separation point, the increase becomes dramatically high due to separation reaching its maximum value at the transition point. For the stalled condition (AOA = 15°), the scenario is completely different and the displacement thickness increases along the entire airfoil suction side as the height of the separated shear layer portion is increased along the airfoil chord.



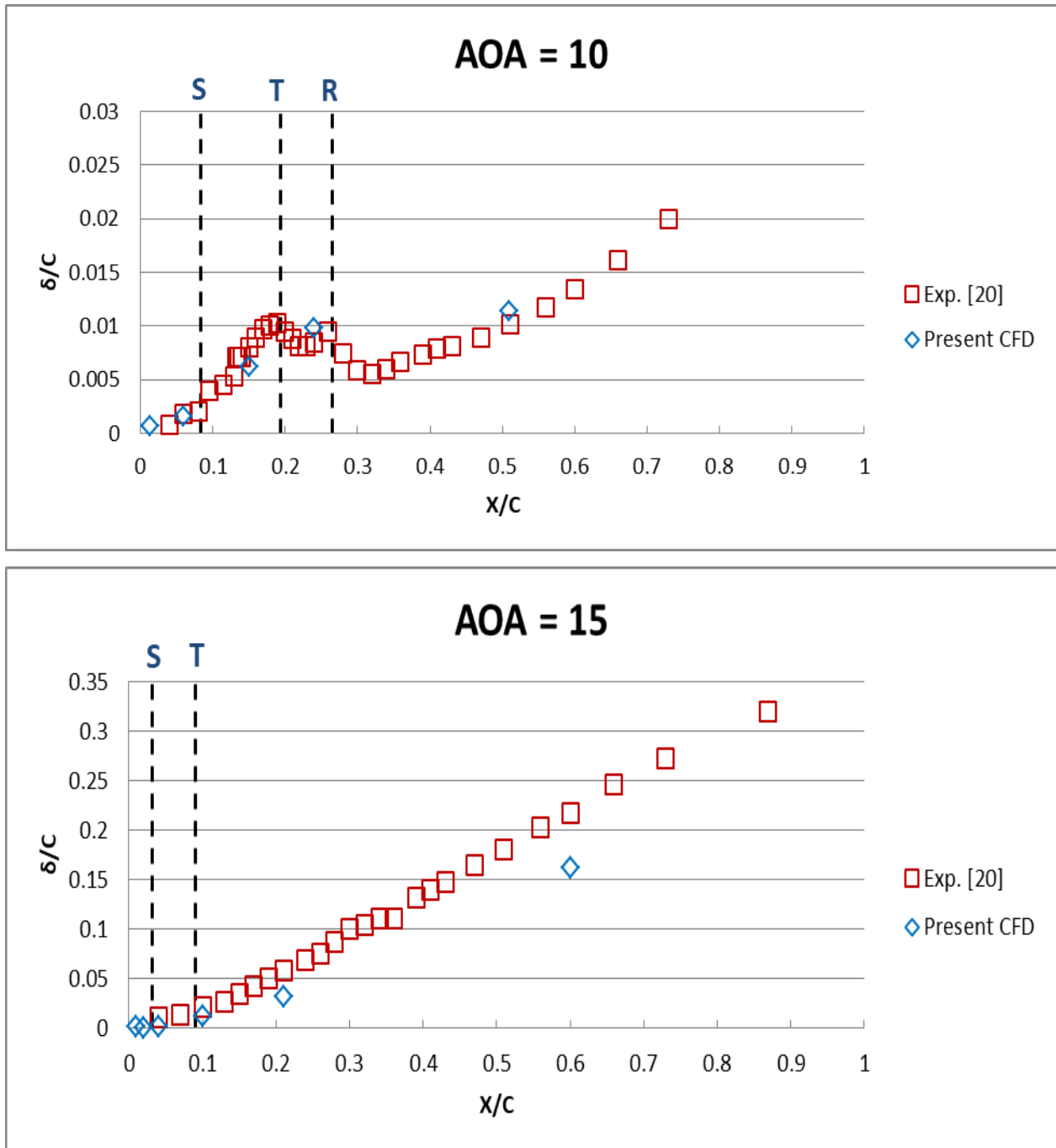
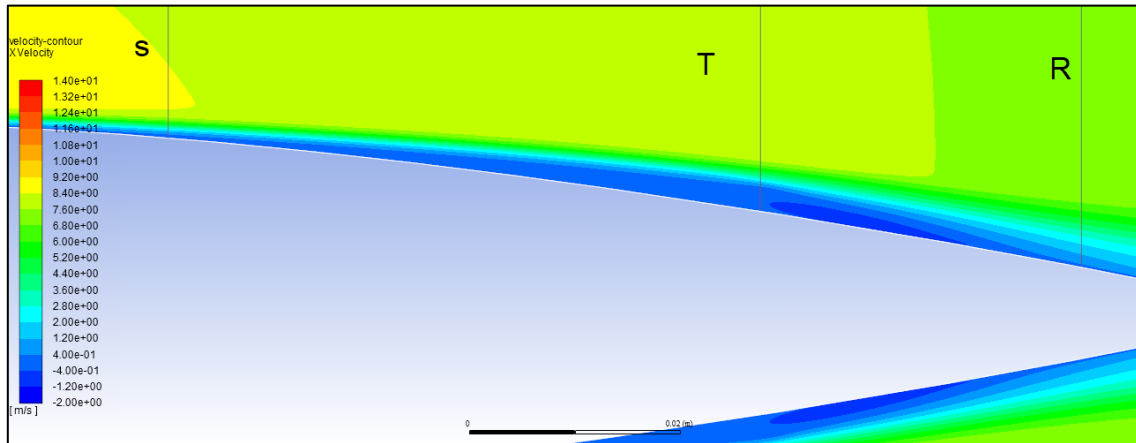
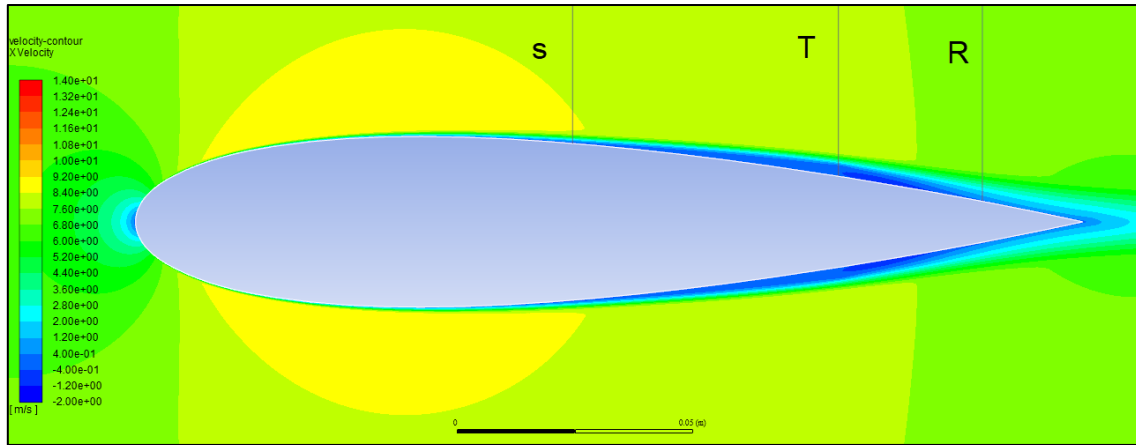


Figure 19: Boundary layer displacement thickness for different AOAs.

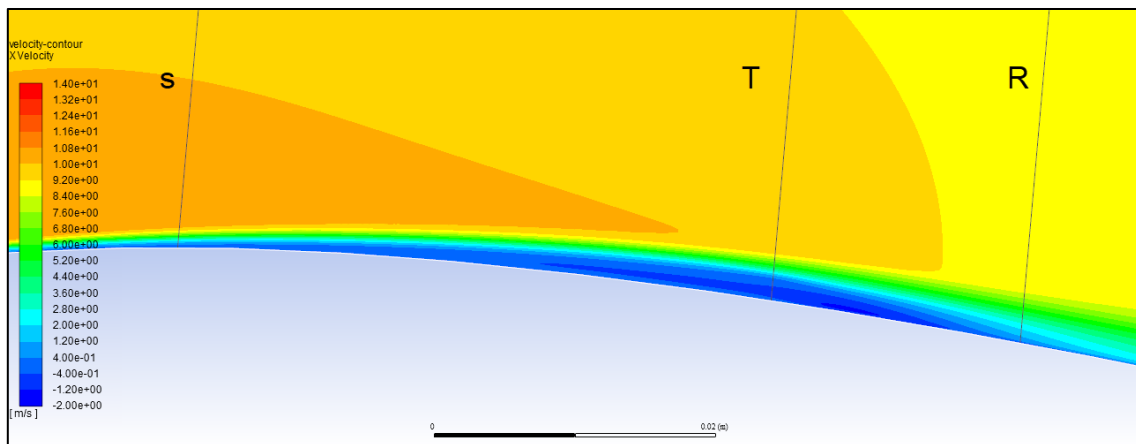
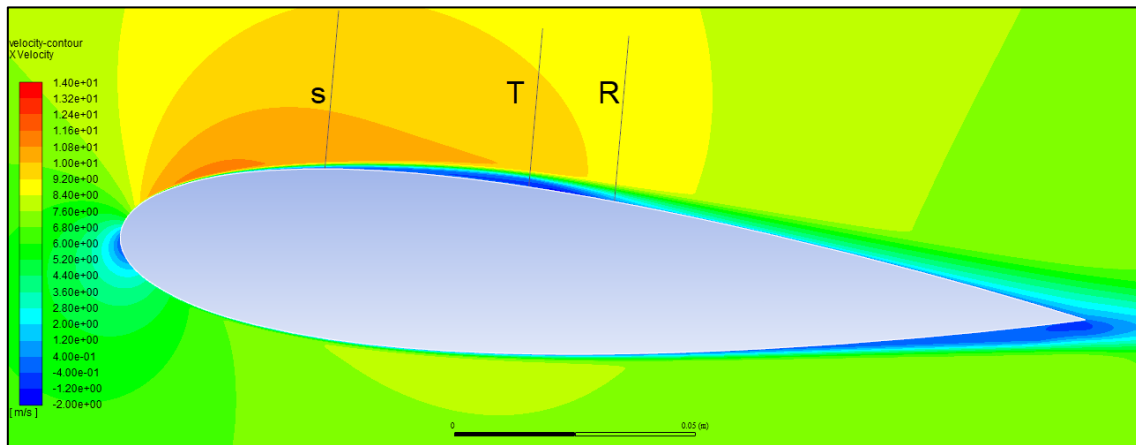
After completing a full boundary layer analysis, the streamwise velocity contours are presented from the simulations in order to be able to visualize the laminar separation bubble formation along the airfoil suction side. The velocity contours for all presented angles of attack are shown in figure 20, where the upper figure for each angle of attack presents the location of the separation bubble along the entire airfoil chord whereas the lower figure shows a close view inside the separation bubble.

Downward the separation point, a region of stagnant flow is initiated on the airfoil surface then the reversed flow appears with negative velocity values. The separation bubble height is gradually increased until reaching the transition point then it returns to decrease again. At the reattachment point, the enhanced mix of the free stream flow is noticed by the presence of faster change in the contours across the reattachment line in the normal direction to the airfoil surface. Whereas for the stalled condition (AOA=15°) the flow is completely separated along the airfoil suction side.

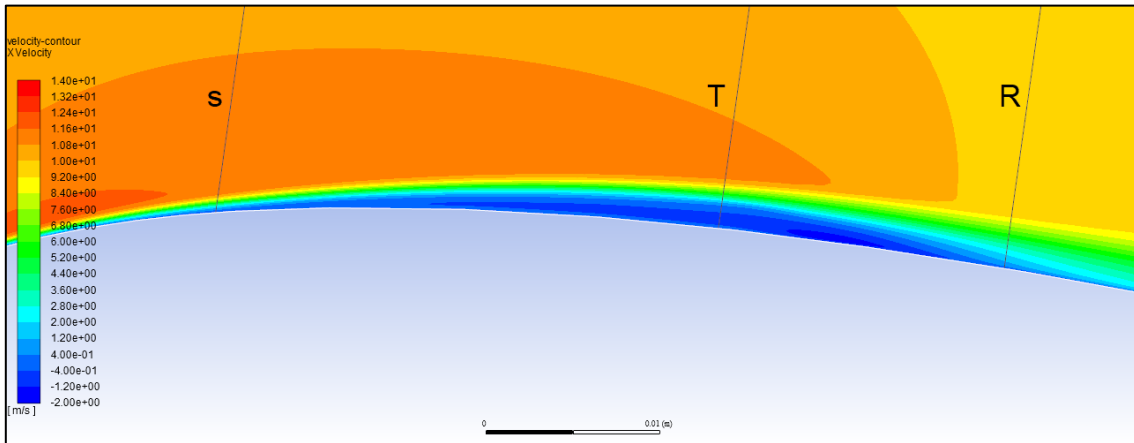
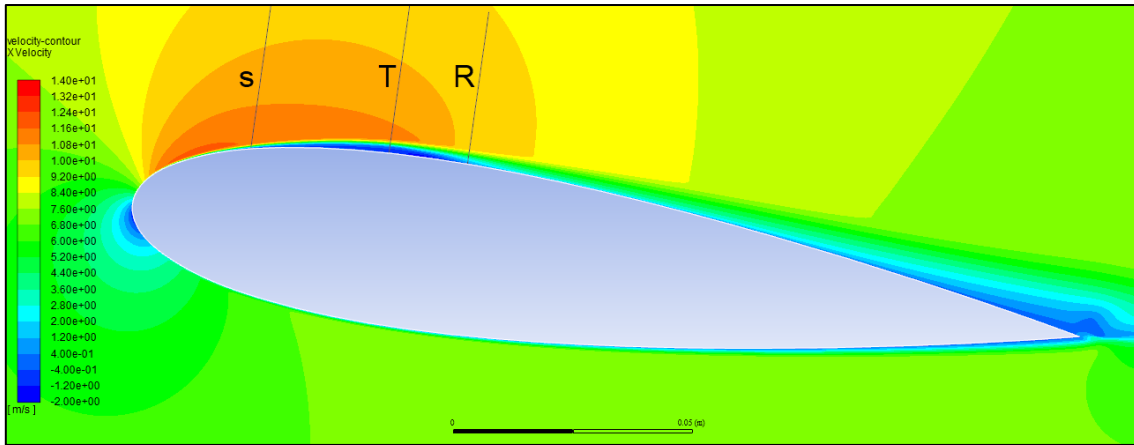
Comparing the developed flow over the airfoil at different angles of attack, as the angle of attack increases, the formed separation bubble moves towards the leading as well as the bubble extent is shortened.



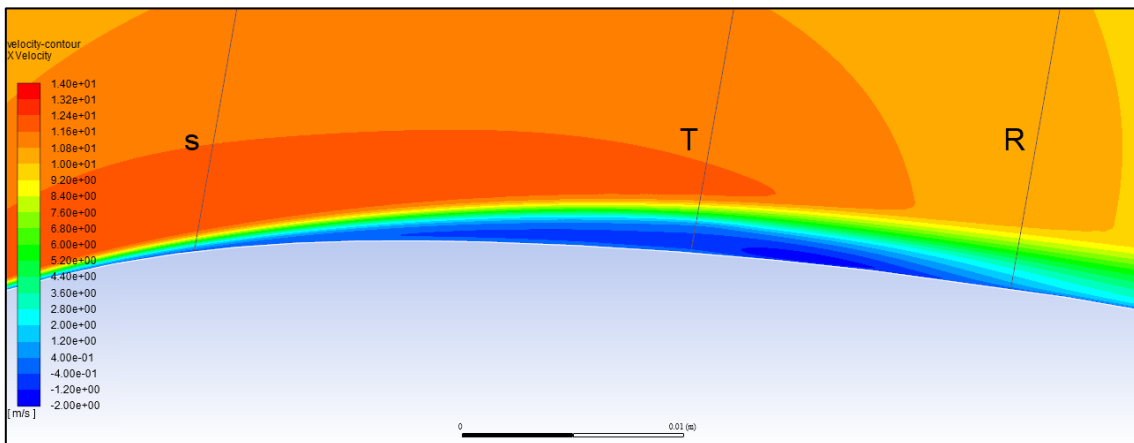
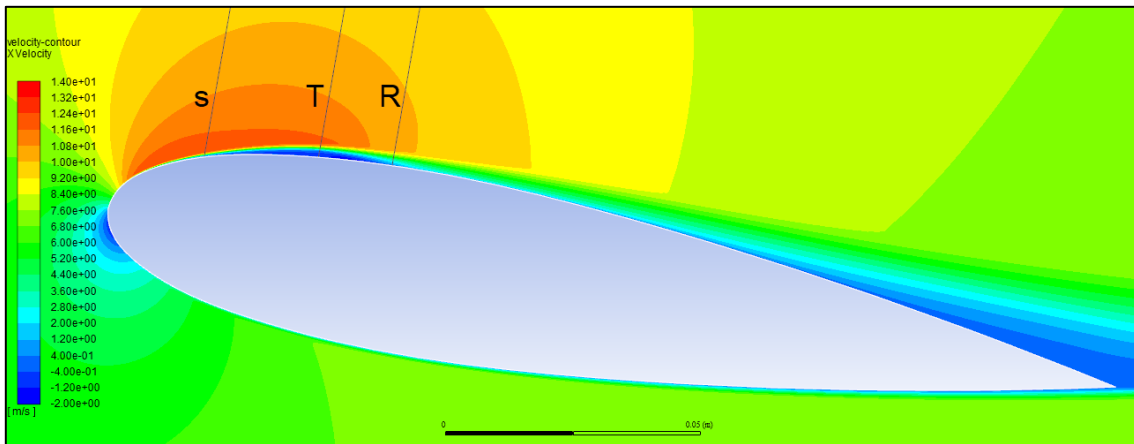
AOA = 0°.



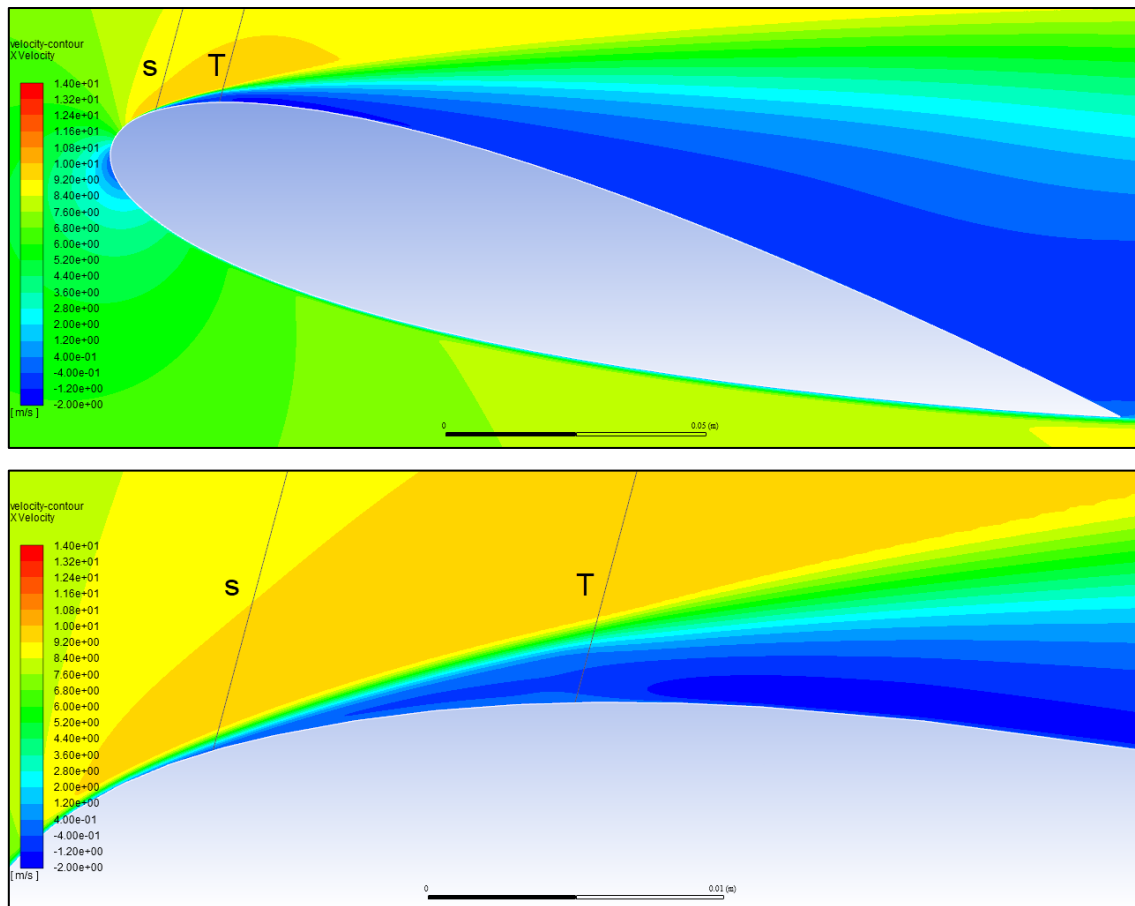
AOA = 5°.



AOA = 8°.



AOA = 10°.



AOA = 15°.

**Figure 20:** X-Velocity contours on the airfoil suction side for different AOA.

#### 4. Conclusion

The present numerical investigation provides precise computational modeling for the transitional flow over low Reynolds number airfoils. The NACA-0018 airfoil section was used for the present study for a Reynolds number of  $10^5$  and at various AOA. Two different computational domains (open filed domain and wall bounded domain) were used for the current study in order to numerically estimate the wind tunnel effect on the developed flow over the airfoil. The computational domain, grid and numerical procedures were optimized to be convenient for the used turbulence model as well as the simulating conditions.

Transition modeling was applied for all simulations using the steady 2D-RANS equations coupled with the  $(\gamma - \tilde{R}e_\theta)$  transition model. Computational results were validated with the available experimental measurements.

The present CFD results are showing very good agreement with the experimental results providing accurate predictions for separation, transition and reattachment locations for the airfoil before the stall angle, otherwise after stall; the predicted computational results were not accurate enough. The predicted skin friction coefficient showed better ability to predict the actual separation, transition and reattachment locations than the estimated locations that were obtained from the surface pressure coefficient, as well as it could clearly identify the location of turbulent separation near the airfoil trailing edge which was not detected in the surface pressure coefficient plot.

The present model also was able to accurately predict the mean velocity profiles, whereas the predicted instantaneous velocity profiles which were calculated from the obtained kinetic energy for each simulation were underestimated compared to the experimental data. All computational simulations showed that the effect of wind tunnel walls is minor for small angles of attack, while this effect is noticeable for relatively high angles. However, the tunnel walls are not affecting any of the separation, transition and reattachment locations.

#### 5. References

- [1] M. Rong, Z. B. Wen, and L. P. Qing, "Optimization design study of low-Reynolds-number high-lift airfoils for the high-efficiency propeller of low-dynamic vehicles in stratosphere," *Sci. China Technol. Sci.*, vol. 53, no. 10, pp. 2792–2807, 2010, doi: 10.1007/s11431-010-4087-0.
- [2] B. E. Prentice, R. E. Beilock, A. J. Phillips, and J. Thomson, "The Rebirth of Airships," *J. Transp. Res. Forum*, vol. 44, no. 1, pp. 173–190, 2010, doi: 10.5399/osu/jtrf.44.1.806.
- [3] H. Schlichting and K. Gersten, "Boundary-Layer Theory," *Boundary-Layer Theory*, pp. 1–799, 2016, doi: 10.1007/978-3-662-52919-5.
- [4] S. M. Berkowitz, "Theory of wing sections," *J. Franklin Inst.*, vol. 249, no. 3, p. 254, 1950, doi: 10.1016/0016-

0032(50)90516-3.

- [5] W. A. Timmer, "Two-dimensional low-Reynolds number wind tunnel results for airfoil NACA 0018," *Wind Eng.*, vol. 32, no. 6, pp. 525–537, 2008, doi: 10.1260/030952408787548848.
- [6] T. Nakano, N. Fujisawa, Y. Oguma, Y. Takagi, and S. Lee, "Experimental study on flow and noise characteristics of NACA0018 airfoil," *J. Wind Eng. Ind. Aerodyn.*, vol. 95, no. 7, pp. 511–531, 2007, doi: 10.1016/j.jweia.2006.11.002.
- [7] S. Yarusevych, P. E. Sullivan, and J. G. Kawall, "Coherent structures in an airfoil boundary layer and wake at low Reynolds numbers," *Phys. Fluids*, vol. 18, no. 4, 2006, doi: 10.1063/1.2187069.
- [8] S. Yarusevych, J. G. Kawall, and P. E. Sullivan, "Unsteady separated flow characterization on airfoils using time-resolved surface pressure measurements," *AIAA J.*, vol. 46, no. 2, pp. 508–516, 2008, doi: 10.2514/1.33306.
- [9] S. Yarusevych, P. E. Sullivan, and J. G. Kawall, "On vortex shedding from an airfoil in low-Reynolds-number flows," *J. Fluid Mech.*, vol. 632, pp. 245–271, 2009, doi: 10.1017/S0022112009007058.
- [10] L. R. Numbers, R. Gerakopoulos, M. S. H. Boutilier, and S. Yarusevych, "Aerodynamic Characterization of a NACA 0018 Airfoil at," no. July, pp. 1–13, 2010.
- [11] M. S. H. Boutilier and S. Yarusevych, "Effects of end plates and blockage on low-Reynolds-number flows over airfoils," *AIAA J.*, vol. 50, no. 7, pp. 1547–1559, 2012, doi: 10.2514/1.J051469.
- [12] F. R. Menter, R. B. Langtry, S. R. Likki, Y. B. Suzen, P. G. Huang, and S. Völker, "A correlation-based transition model using local variables - Part I: Model formulation," *J. Turbomach.*, vol. 128, no. 3, pp. 413–422, 2006, doi: 10.1115/1.2184352.
- [13] N. N. Sørensen, "CFD modelling of laminar-turbulent transition for airfoils and rotors using the  $\gamma$ - $R_{\theta}$  model," *Wind Energy*, vol. 12, no. 8, pp. 715–733, 2009, doi: 10.1002/we.325.
- [14] B. Akay, D. Ragni, C. S. Ferreira, and G. J. W. Van Bussel, "Investigation of the root flow in a Horizontal Axis," *Wind Energy*, no. April 2013, pp. 1–20, 2013, doi: 10.1002/we.
- [15] K. A. Fagbenro, M. A. Mohamed, and D. H. Wood, "Computational modeling of the aerodynamics of windmill blades at high solidity," *Energy Sustain. Dev.*, vol. 22, no. 1, pp. 13–20, 2014, doi: 10.1016/j.esd.2013.12.011.
- [16] H. Shah, S. Mathew, and C. M. Lim, "Numerical simulation of flow over an airfoil for small wind turbines using the  $\gamma$ - $Re_{\theta}$  model," *Int. J. Energy Environ. Eng.*, vol. 6, no. 4, pp. 419–429, 2015, doi: 10.1007/s40095-015-0188-7.
- [17] J. Morgado, R. Vizinho, M. A. R. Silvestre, and J. C. Páscoa, "XFOIL vs CFD performance predictions for high lift low Reynolds number airfoils," *Aerosp. Sci. Technol.*, vol. 52, pp. 207–214, 2016, doi: 10.1016/j.ast.2016.02.031.
- [18] P. C. S. Kapsalis, S. Voutsinas, and N. S. Vlachos, "Comparing the effect of three transition models on the CFD predictions of a NACA0012 airfoil aerodynamics," *J. Wind Eng. Ind. Aerodyn.*, vol. 157, pp. 158–170, 2016, doi: 10.1016/j.jweia.2016.07.007.
- [19] R. B. Langtry, F. R. Menter, S. R. Likki, Y. B. Suzen, P. G. Huang, and S. Völker, "A correlation-based transition model using local variables - Part II: Test cases and industrial applications," *J. Turbomach.*, vol. 128, no. 3, pp. 423–434, 2006, doi: 10.1115/1.2184353.
- [20] M. S. H. Boutilier, "Experimental Investigation of Transition over a NACA 0018 Airfoil at a Low Reynolds Number," *Thesis*, 2011.
- [21] R. Gerakopoulos and S. Yarusevych, "Novel time-resolved pressure measurements on an airfoil at a low Reynolds number," *AIAA J.*, vol. 50, no. 5, pp. 1189–1200, 2012, doi: 10.2514/1.J051472.
- [22] T. M. Kirk, "The Later Stages of Transition over a NACA0018 Airfoil at a Low Reynolds Number," *Thesis*, 2014.
- [23] R. B. Langtry and F. R. Menter, "Correlation-based transition modeling for unstructured parallelized computational fluid dynamics codes," *AIAA J.*, vol. 47, no. 12, pp. 2894–2906, 2009, doi: 10.2514/1.42362.
- [24] R. B. Langtry, J. Gola, and F. R. Menter, "Predicting 2D Airfoil and 3D Wind Turbine Rotor Performance using a Transition Model for General CFD Codes," *Sci. York*, vol. 2006, no. January, pp. 1–11, 2006.
- [25] S. V. Patankar and D. B. Spalding, "A calculation procedure for heat, mass and momentum transfer in three-dimensional parabolic flows," *Int. J. Heat Mass Transf.*, vol. 15, no. 10, pp. 1787–1806, 1972, doi: 10.1016/0017-9310(72)90054-3.
- [26] W. Shyy, S. Thakur, and J. Wrightt, "Second-order upwind and central difference schemes for recirculating flow computation," *AIAA J.*, vol. 30, no. 4, pp. 923–932, 1992, doi: 10.2514/3.11010.
- [27] J. Blazek, "Consistency, Accuracy, and Stability," *Comput. Fluid Dyn. Princ. Appl.*, pp. 337–356, 2015, doi: 10.1016/b978-0-08-099995-1.00010-5.
- [28] F. R. Menter, "Two-equation eddy-viscosity turbulence models for engineering applications," *AIAA J.*, vol. 32, no. 8, pp. 1598–1605, 1994, doi: 10.2514/3.12149.
- [29] L. Du, "Numerical and Experimental Investigations of Darrieus Wind Turbine Start-up and Operation," *PQDT - UK Irel.*, 2015.
- [30] M. S. H. Boutilier and S. Yarusevych, "Parametric study of separation and transition characteristics over an airfoil at low Reynolds numbers," *Exp. Fluids*, vol. 52, no. 6, pp. 1491–1506, 2012, doi: 10.1007/s00348-012-1270-z.
- [31] M. M. O'Meara and T. J. Mueller, "Experimental Determination of the Laminar Separation Bubble Characteristics of an Airfoil At Low Reynolds Numbers.," *AIAA Pap.*, vol. 25, no. 8, 1986, doi: 10.2514/6.1986-1065.
- [32] P. K. Kundu, I. M. Cohen, and D. R. Dowling, *Boundary Layers and Related Topics*. 2016.
- [33] M. Brendel and T. J. Mueller, "Boundary-layer measurements on an airfoil at low Reynolds numbers," *J. Aircr.*, vol. 25, no. 7, pp. 612–617, 1988, doi: 10.2514/3.45631.

---

## Nomenclature

2D: two dimensional

AOA: angle of attack

ASW: aerodynamic straight wall

CFD: computational fluid dynamics

GSW: geometric straight wall  
LSB: laminar separation bubble  
RANS: Reynolds averaged Navier-Stokes  
RMS: root mean square  
SST: shear stress transport  
C: chord length  
 $C_D$ : drag coefficient  
 $C_f$ : skin friction coefficient  
 $C_L$ : lift coefficient  
 $C_p$ : surface pressure coefficient  
K: turbulent kinetic energy  
 $Re$ : chord based Reynolds number  
 $\tilde{Re}_\theta$ : local transition onset momentum thickness Reynolds number  
 $Tu$ : turbulence intensity  
U: local mean velocity  
 $U_\infty$ : free stream velocity  
 $\tilde{u}$ : local RMS velocity  
X: chord streamwise location  
Y: chord transverse location  
 $y$ : distance to nearest wall  
 $\gamma$ : intermittency  
 $\delta$ : boundary layer thickness  
 $\mu$ : molecular viscosity  
 $\mu_t$ : eddy viscosity  
 $\rho$ : density  
 $\nu$ : dynamic viscosity  
 $\omega$ : specific turbulence dissipation rate  
 $\tau_w$ : wall shear stress

**Subscripts**

S: Separation  
T: Transition  
R: Reattachment